

An Ultraviolet Laser for Beryllium Photoionization

Christian Michael Pluchar

Advisor: Professor David A. Hanneke
May 1, 2018

Submitted to the
Department of Physics & Astronomy of Amherst College
in partial fulfillment of the
requirements for the degree of
Bachelors of Arts with honors

© 2018 Christian Michael Pluchar

Abstract

Trapped ions are attractive systems for quantum state manipulation and detection, and have been used for quantum information processing, precision measurement, and optical atomic clocks. The beryllium ion is a popular choice in these experiments, but a method is needed for efficiently ionizing neutral beryllium and loading it into a trap. This thesis describes the design and construction of an ultraviolet laser capable of ionizing neutral beryllium atoms. The UV light produced has a wavelength of 235 nm and is resonant with the $2s$ to $2p$ transition in neutral beryllium. A second 235 nm photon ionizes the atom once in the excited state. The resonant step of the two-photon process selectively ionizes beryllium atoms.

Blue light with a wavelength of 470 nm from a commercial external cavity diode laser is passed through a nonlinear crystal (beta barium borate), which generates the second harmonic, producing 235 nm light. To increase UV production, a power enhancement cavity was built around the nonlinear crystal. The custom monolithic cavity provides additional isolation from vibration and environmental disturbances. To lock the cavity on resonance, a feedback loop using photodetectors and a FPGA servo was assembled.

The system generates over 300 μW of ultraviolet light, enough to saturate the $2s$ to $2p$ transition over a small area of beryllium atoms and ionize them at a modest rate. In the future, improving the coupling into the power enhancement cavity will increase the UV power output to 25 mW, which will produce ions at a faster rate. The laser system will also be used to photodissociate O_2^+ .

Acknowledgments

First and foremost, thank you to Professor Hanneke. I am so very grateful for the many hours you spent with me in lab, explaining concepts to me, and reading over drafts. You have a way of bringing out my best work, and I left every meeting feeling confident I could finish this work. From iLab to the last week of my thesis, some of my favorite and most influential parts of my Amherst Physics experience has been due to your guidance.

Designing and manufacturing the monolithic cavity would not have been possible without the help of Jim Kubasek. Thank you for helping me learn SolidWorks, and develop a certain style of thinking about the assembly and components. These skills were invaluable for such a complex project. The hours you spent to get the parts precisely machined, as well as tackling the difficult angled cuts and exterior cuts for the mirror mounts is appreciated.

Ryan Carollo was a steady presence in helping me throughout the project. Thank you for going out of your way to help me with the experimental work, lending eyes and ears to problems, most notably the cavity coupling, giving me advice and encouragement, as well as providing feedback and helping me with cavity design decisions.

Thank you to Brian Creapeau, who helped me troubleshoot and repair the

FPGA servo which will become the brains for locking the cavity.

Thank you to all my friends, especially those who listened to me talk about “lazars.” Thank you to my teammates past and present who supported me for the last two months. Thanks and congratulations to my fellow senior Physics Majors, who have been kind and supportive, and each of which has made a mark on my time here.

Finally, thank you to my family for supporting me through college, encouraging me, and always being there for me.

This material is based upon work supported by the Amherst College Dean of the Faculty and by the National Science Foundation under CAREER grant number PHY-1255170. Thank you to the Thomases Family, Baines Family, and the Gregory S. Call Student Research Fund for helping support me and my work.

Contents

1	Introduction	1
1.1	Versatile Uses for Trapped Ions	1
1.1.1	Searching for New Physics	3
1.2	Generating 235 nm Light	5
2	Theory of Second Harmonic Generation	10
2.1	Gaussian Beams	10
2.2	External Cavity Diode Lasers	14
2.2.1	Semiconductor Laser Fundamentals	14
2.2.2	External Cavity Diode Lasers	19
2.3	Second Harmonic Generation	22
2.4	Optimal Second Harmonic Generation in Beta Barium Borate	26
2.4.1	Birefringent Phase Matching in BBO	27
2.4.2	Optimal Focusing and Walkoff in BBO	30
2.5	Optical Resonators	31
2.5.1	Power Enhancement	35
2.5.2	Impedance Matching	39
3	Building and Optimizing the Cavity	41
3.1	Monolithic Cavity Design in Solidworks	41
3.2	Input Optics	43
3.3	Generating UV Light from a Single Pass	48
3.4	Aligning the Cavity and Mode Matching	50
4	Next Steps	53
4.1	Theoretical Rate for Photoionizing Beryllium with the Present Power Output	53
4.2	Improved Cavity Performance	54
4.3	Locking the Cavity	56
4.4	Laser Frequency Stability	61

4.5 Conclusion	62
A Monolithic Cavity Design	64

List of Figures

1.1	Scheme for Photoionizing Beryllium	2
1.2	Oxygen Photodissociation	6
1.3	Trapped Beryllium Ions	7
2.1	Mode Hopping	21
2.2	Potentials	24
2.3	Symmetric Bowtie Cavity	35
2.4	SHG Power Vs Input Power	38
2.5	Impedance Matching	40
3.1	Cavity Design with Beam Path	43
3.2	Beryllium Photoionization Laser System	44
3.3	Beam Circularization	45
3.4	Oscilloscope Trace of Scanning Through Resonance	51
3.5	Oscilloscope Trace of Blue and UV Buildup	52
4.1	Spot size as a Function of Lens Separation	56
4.2	Circulating Power versus UV Output Power	57
4.3	Reflected Power versus Frequency	58
4.4	ECDL Frequency Measurement	62
A.1	SolidWorks Rendering of the Cavity	64
A.2	SolidWorks Rending of the Cavity with Crystal Aligner Removed	65
A.3	SolidWorks Rendering of the Cavity's Internal Design	65
A.4	Machined Cavity	66
A.5	Crystal Mount and BBO Crystal	67
A.6	Cavity Internal View	68
A.7	Top View of the Cavity	69
A.8	Cavity Exterior	70
A.9	Cavity and Input Optics	71

Chapter 1

Introduction

1.1 Versatile Uses for Trapped Ions

Precisely controlling individual atoms and molecules has enabled a new range of experiments to precisely measure the behavior of matter. Techniques for trapping and manipulating atomic and molecular ions have been at the forefront of research for improving precision measurement techniques, and lead to sympathetic cooling of co-trapped atoms [1], advances in quantum information processing, quantum simulation, and progress towards a general purpose quantum computer [2], as well as building more precise atomic clocks operating at optical frequencies [3]. Many of these advances have utilized beryllium ions because of its single valence electron when ionized and a closed cyclic transition which is ideal for laser cooling. This thesis describes the design and implementation of a laser to ionize neutral beryllium. The two-photon ionization scheme employed (Fig. 1.1) requires ultraviolet light at a wavelength

where few commercial lasers are available. Instead, a power enhancement cavity around a nonlinear crystal is used to generate the second harmonic of a pump beam from an external cavity diode laser. This method promises to improve the speed and efficiency of the loading process over electron-impact ionization, the current technique used. Additionally, this method is selective, so only beryllium is ionized and loaded into the trap.

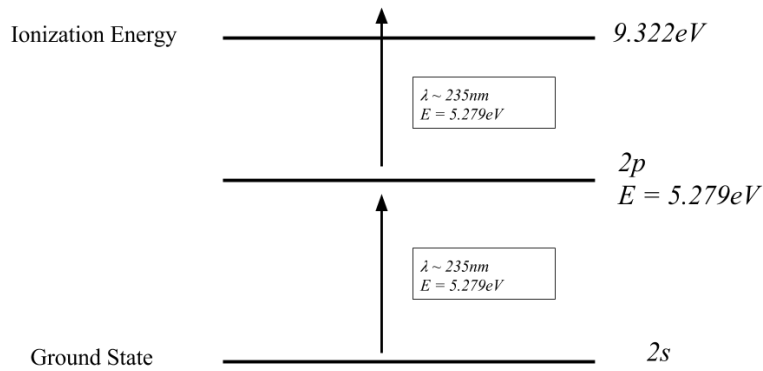


Figure 1.1: Two-photon ionization scheme for beryllium. To photoionize neutral beryllium, one photon at the resonant transition frequency will move it between the 2s and 2p state. A second photon from the same laser will then move the electron to the continuum.

The experimental apparatus is centered around a Paul (radiofrequency) Trap. Earnshaw's Theorem prohibits the existence of a configuration of static electric fields to confine a particle. Instead, a Paul trap uses a combination of stationary and oscillating electric fields to confine charged particles to a limited area of space so they can be studied over a longer duration of time [4]. The contents of the trap are in vacuum, isolating the trap contents from external interactions. Paul traps are versatile compared with other commonly used

trapping techniques, such as magneto-optical traps. Multiple particle species, including molecules, can be trapped with identical trap parameters, and can even be trapped simultaneously. This enables an entire range of new techniques to be utilized and particle interactions to be studied.

In our apparatus, co-trapping ions enables us to use beryllium ions to sympathetically cool diatomic oxygen ions. Laser cooling ions to their ground state places them closer to the trap center and eliminates the first order Doppler shift. The strong cyclic transition in Be^+ makes it ideal for laser cooling. However, not all ions have a good laser cooling transition, but sympathetically cooling these ions using beryllium has become a well developed technique [1]. The Coulomb force between the two species of ions allows the beryllium atom to dampen the vibrations of the co-trapped ion, reducing its temperature.

1.1.1 Searching for New Physics

The primary motivation for this work is to measure the time dependence of fundamental “constants.” Using precision measurement techniques in a small laboratory environment to measure fundamental constants has received attention recently because it offers an alternative method to particle accelerators and other large, costly experiments to test certain fundamental theories [5]. One particular fundamental constant of interest is the ratio of the mass of the proton to the mass of the electron (m_p/m_e , or μ). Observations of molecular absorption lines in gas clouds from light emitted by quasars have indicated a possible drift in the value of μ on cosmological time scales [6]. This is an intriguing finding, as the time variation of μ is an important feature of some

theories of physics beyond the Standard Model, and may indicate the existence of additional spatial dimensions [7], or the presence and interaction with a scalar or pseudoscalar dark matter field [8]. The strong nuclear force, which binds quarks together to form protons, sets the mass of the proton, and the electroweak force sets the mass of the electron, so observing a change in μ could indicate the relative strength of the strong and electroweak forces is changing over time [6]. While the astronomical observations are not precise enough to draw any definitive conclusions about a nonzero variation in μ , by employing a different approach and eliminating systematic errors with a laboratory experiment, it is feasible to measure possible variations in μ by measuring the energy levels of vibrational transitions in diatomic molecules [6]. Over the past few years, the Hanneke Ion Trap Lab has been designing and building an apparatus to measure the time variation of the proton-to-electron mass ratio. The work presented in this thesis builds upon previous efforts by Professor Hanneke, numerous other scientists, and previous thesis students in order to reach this goal.

The separation in energy between vibrational states in diatomic molecules is dependent on the proton to electron mass ratio. The mass of the proton helps set the mass of the nuclei, while chemical bond strength, and therefore the separation between the nuclei, is a function of the electron mass. O_2^+ has been identified as having relatively high sensitivity to variations in μ , low sensitivity to systematic errors, and transitions which are in a wavelength range which is accessible by readily available technology [9]. The transition from the $v = 0$ vibrational state to the $v = 11$ is particularly attractive. The

outline for the proposed method to detect changes in μ is to tune a laser to be resonant with this transition and measure its change over a year. By comparing the frequency of the resonant light relative to a known, stable frequency, the variation in the energy difference between the two states can be measured. The experimental setup and design of the apparatus mitigates any systematic effects. The $v = 0$ to $v = 11$ transition has a small linewidth because it is electric-dipole forbidden. Additionally, the O_2^+ will be cooled to minimize the Doppler broadening of the transition, and ion trap has been placed in an ultra-high vacuum to mitigate interactions with other particles.

To verify the trapped O_2^+ have been placed in the higher vibrational state, the UV laser described here will be used to dissociate the ions. When in the 11th vibrational state, the dissociation energy is equivalent to the energy of a 238 nm photon. A 235 nm photon, with slightly higher energy, will have sufficient energy to dissociate O_2^+ into O and O^+ (Fig. 1.2), but not enough to dissociate diatomic oxygen ions in the ground vibrational state. A time of flight mass spectrometer will determine the ratio of O^+ to O_2^+ , which is directly proportional to the ratio of trapped O_2^+ the $v = 11$ versus the $v = 0$ vibrational state.

1.2 Generating 235 nm Light

In order for particles to be loaded into the Paul trap, they must be electrically charged. Multiple methods exist to ionize atoms and molecules. Previously, our lab utilized an electron gun to ionize the beryllium atoms. Electrons

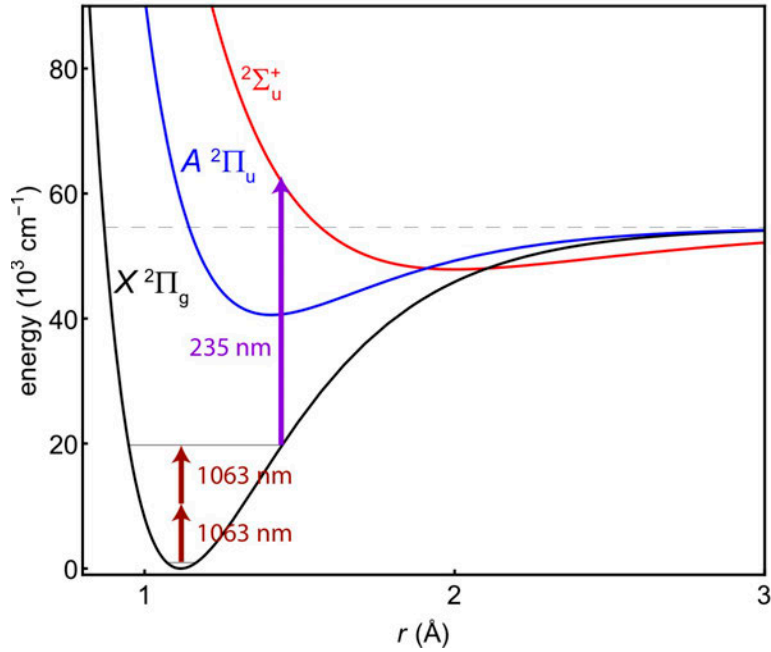


Figure 1.2: Bond energy versus separation for different electronic states in oxygen molecules. Oxygen is moved from the $v = 0$ vibrational state to $v = 11$ with two 1063 nm photons. When in this state, a single 235 nm photon can alter the electronic state, and move an electron from the $X^2\Pi_g$ state to the $^2\Sigma_u^+$ state. In doing so, the electron exceeds the dissociation energy (dashed line), breaking the bond between the two oxygen nuclei. Figure courtesy David Hanneke.

emitted from the electron gun incident on a cloud of neutral beryllium gas have enough energy to remove a valence electron from the atom. While this method ionizes the beryllium atoms, it also ionizes surrounding atoms and molecules present with the beryllium gas. The system has been placed in an ultra-high vacuum chamber to limit the number of external interaction with the beryllium ions, however the current method introduces additional particles into the trap. Furthermore, collisions with the electron beam heat

up the contents of the trap. The additional energy this introduces is sufficient to limit the number of ions which can be trapped at any one time. The rate at which the ions can be loaded is slow, and future experiments will need to quickly load, dump, and reload ions.

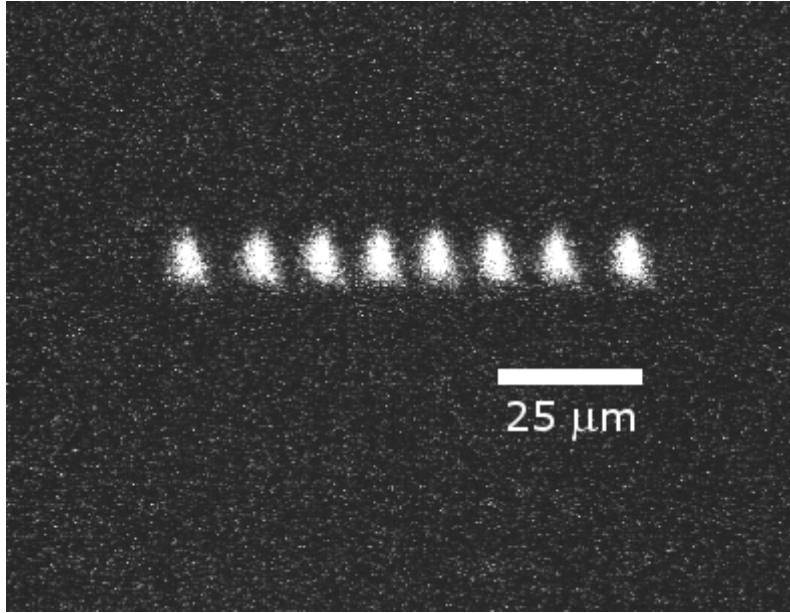


Figure 1.3: Beryllium ions trapped in the Paul Trap. The ions have been sufficiently cooled to the point where they form a Coulomb crystal, and the ions do not have sufficient energy to swap places with their neighbor in the lattice. Figure courtesy David Hanneke.

Ionizing using laser light avoids many of these problems. If we were to try to ionize neutral beryllium atoms with a single photon, it would require a photon with an energy which exceeds the beryllium ionization energy of 9.3 eV (or $\lambda = 133$ nm). Because this wavelength is very short and falls in a region which it is challenging to develop suitable optics for (the “vacuum UV”), a two photon ionization scheme, and therefore a longer laser wavelength,

is preferable. Additionally, the single photon ionization scheme has enough energy to ionize surrounding atoms other than beryllium, while the two photon scheme selectively ionizes only the beryllium. Specifically, the system will produce a photon which is resonant with the $2s$ to $2p$ transition. A second photon of the same frequency can ionize the atom.

The wavelength of light needed in vacuum is 234.9329 nm [10], which is in the deep ultraviolet. This wavelength not accesible by any readily available laser diodes (see Section 2.2). However, the development of nonlinear optics has enabled the generation of frequencies of laser light which were previously unattainable. To a first order approximation, most materials display a polarization which is proportional to the electric field of an incident electromagnetic wave. Nonlinear materials have large coefficients for higher-order terms, and when combined with large intensities, a significant portion of the fundamental frequency can be converted into higher harmonics (see Section 2.3). A number of nonlinear processes have been developed, including second harmonic generation (generating twice the fundamental frequency), sum-frequency generation (generating the sum of two input frequencies), and differnce-frequency generation (generating the difference of two input frequencies). Nonlinear techniques are currently used in the Hanneke Ion Trap lab to generate 313 nm light from a readily available 940 nm external cavity diode laser using both second harmonic generation and sum frequency generation to produce the third harmonic [11]. This laser frequency is used for Doppler cooling the beryllium atoms. While other systems have been developed to produce 235 nm light by doubling 940 nm twice [12]. Instead, our approach uses a commercially

available 470 nm external cavity diode laser and the required 235 nm light can be produced using just a single stage of second harmonic generation, reducing the complexity of the system. The external cavity diode laser is tunable so it can be resonant with the desired transition in beryllium (Section 2.2.2). In order to increase UV output, a power enhancement cavity was also built. The optical resonator increases the power of the light passing through the crystal. It is common to increase the power of the input beam by a factor of 100 (Section 2.5). Because the amount of power generated at the second harmonic increases quadratically with the input beam power (see Eq. 2.20), employing the optical resonator can often increase the SHG output by orders of magnitude over just using a single pass.

The notable improvement of this system is the monolithic cavity which forms the optical resonator. Previous studies have shown the vibration tolerance of the optical resonator can be improved and its time spent locked can be significantly increased by constructing the enclosure out of a single block of aluminium [13]. A monolithic cavity was designed and built as part of this thesis. Cool, dry air is continuously pumped into the airtight enclosure to keep contaminants from depositing on the surfaces of the optics.

Chapter 2

Theory of Second Harmonic Generation

This chapter will describe the theoretical basis behind the ultraviolet laser system, particularly second harmonic generation and considerations for optimizing UV production. Basic Gaussian beam theory is covered which provides the basis for the discussion on optical resonators and optimal focusing in the nonlinear crystal. I aim to motivate the design decisions, such as utilizing second harmonic generation, building a power enhancement cavity, and selecting an external cavity diode laser to generate the pump beam.

2.1 Gaussian Beams

Gaussian beam theory provides a suitable approximation for beam propagation [14]. In most circumstances, the wavefront of the beam can be approximated as being close to a plane wave (a flat wavefront). We can find spatial

intensity profiles which satisfy the paraxial wave equation

$$\frac{\delta^2 \psi}{\delta x^2} + \frac{\delta^2 \psi}{\delta y^2} - 2ik \frac{\delta \psi}{\delta z} = 0, \quad (2.1)$$

which utilizes this assumption. The solutions can be written in the form of

$$u(x, y, z) = \psi(x, y, z)e^{-ikz}, \quad (2.2)$$

where $\psi(x, y, z)$ is the magnitude of the electric field of the wave at different points in space. The Hermite-Gaussian modes are one family of solutions which satisfy the paraxial wave equation and form a complete orthogonal set. They describe the strength of the electric field across any beam as a linear combination of the different modes. They take the form of

$$u(x, y, z)_{nm} = \frac{1}{\sqrt{1 + (z/z_R)^2}} H_n(\sqrt{2}\frac{x}{\omega}) H_m(\sqrt{2}\frac{y}{\omega}) \times \exp \left\{ -i(kz - \Phi(m, n; z)) - i\frac{k}{2q}(x^2 + y^2) \right\}, \quad (2.3)$$

where H_n and H_m are the Hermite polynomials of order n and m and $\Phi(m, n; z) = (n + m + 1) \tan^{-1}(\frac{z}{z_R})$, and is known as the Guoy phase. For most purposes it is useful to consider only the lowest order mode, when $n = m = 0$:

$$u(x, y, z) = \frac{1}{\sqrt{1 + (z/z_R)^2}} \exp \left\{ i \tan^{-1} \left(\frac{z}{z_R} \right) - ik \left(z + \frac{r^2}{2R} \right) - \frac{r^2}{\omega^2} \right\}, \quad (2.4)$$

where z_R is the Raleigh range, q is the complex beam parameter, and ω is the spot size. The intensity distribution of this beam is approximately Gaussian

shaped in both the x and y dimensions. Some useful properties of Gaussian beams can be described from this equation. As the beam propagates through space, the spatial field distribution will remain the same shape, but scales in size. The spot size (ω) is equal to the distance from the point of maximum intensity to the point intensity drops to $1/e^2$ of the maximum. The spot size is minimized at the waist (ω_0) when $R = \infty$, where the wavefront is perfectly flat. How rapidly the beam diverges is given by Rayleigh range of the beam (z_R), and is defined as the distance between the waist and the point where the spot size of the beam is a factor of $\sqrt{2}$ larger than the waist. This definition is equivalent to

$$z_R = \frac{\pi\omega_0^2}{\lambda}, \quad (2.5)$$

where λ is the wavelength in the medium the beam propagates in. For the paraxial approximation to hold, the wavefront of the beam must remain approximately flat. Within the Rayleigh range of the beam, the divergence angle of the beam is small.

A useful quantity in determining how various parameters of the beam evolve is the complex beam parameter q , which is given by

$$\frac{1}{q} = \frac{1}{R} - i\frac{\lambda}{\pi\omega^2}, \quad (2.6)$$

where R is the wavefront radius. The z -dependence is remarkably simple, which helps in determining the beam parameters in going from one position to another:

$$q(z) = q_0 + z \quad (2.7)$$

R can be found by examining only the real portion of Eq. 2.6,

$$R = \frac{1}{\operatorname{Re}\{1/q\}} \quad (2.8)$$

while the imaginary portion helps determine the spot size:

$$\omega = \sqrt{\frac{-\lambda}{\pi \operatorname{Im}\{1/q\}}}. \quad (2.9)$$

The position of the waist can be found by observing when the wavefront becomes flat, which corresponds to when the real part of q goes to zero ($R = \infty$), for which the remaining term can be solved for the radius to the waist. Using Eq. 2.7 to extrapolate this to any point, the waist radius will be

$$\omega_0 = \sqrt{-\frac{\lambda \operatorname{Im}\{1/q\}}{\pi |1/q|^2}}. \quad (2.10)$$

Higher order modes (where n or m in Eq. 2.3 are greater than 0) also follow the behavior outlined here, but because of their more complicated field distributions, are usually more difficult to usefully employ. Optical resonators, such as in lasers, are often designed to support the lowest order mode. While the Gaussian mode will contain the majority of the energy in most laser outputs, but there will be smaller contributions from higher order modes as well. It is notable for the treatment of resonators that higher order modes also change the resonant frequency by changing the Gouy phase (Eq. 2.37).

2.2 External Cavity Diode Lasers

2.2.1 Semiconductor Laser Fundamentals

Lasers (Light Amplification by Stimulated Emission Radiation) are devices capable of producing high intensities of monochromatic, coherent light using stimulated emission, making them ideally suited for producing large intensities of light at a specific frequency. While there are a number of different methods to accomplish this, lasers share a few common characteristics, including a gain medium, pumping mechanism, and optical resonator. The basic operating principles of lasers will be described in the context of a diode laser, which will be used in this project. Other types of lasers, like solid-state or gas lasers, operate on similar principles [15].

The electronic states of semiconductors consist of “bands” of allowable electron energies and “gaps” of forbidden energies due to electron wavefunctions satisfying the boundary conditions imposed by the periodic spacing of the atoms in the crystal lattice. The minimum separation in energy between the lower (valence) energy band and the larger (conduction) band is known as the bandgap energy. Impurities in the crystal lattice can impose slightly different boundary conditions to the wavefunctions, which causes local changes to the bandgap energy. This property has been strategically used to change the bandgap of the bulk material by introducing specifically chosen impurities in a process known as doping. There are two common varieties of doping: doping the semiconductor lattice with an element which has one too few valence electrons, and doping with an element which has one too many. The former

are known as acceptor impurities, because they attract electrons, while the latter are donor impurities. A material which has donor impurities added is known as an n -type semiconductor, while p -type semiconductors have acceptor impurities added.

Laser diodes are made by sandwiching a n -type and p -type pieces of a semiconductor together in the same crystal [16]. When the materials are in thermal equilibrium, the charge donors on one side and acceptors on the other cause charges to move across boundary to create a positive charge density adjacent to the n -type side, and a negative charge density next to p -type side. This forms an electric field in what is referred to as the depletion region, and the field points from the n -doped to p -doped side. The electric potential function between the two sides has a difference between the maximum and minimum of the function which is dependent on the materials and their relative proportions in the lattice. If electrons are injected to the p -doped side at a sufficient voltage (forward bias), electrons are able to recombine with positive charges, known as holes. We can observe that reverse biasing the diode prevents charges from flowing due to the electric field in the depletion region. The recombination between holes and electrons results in the release of energy which is equivalent to the bandgap energy.

The bandgap is a function of the crystal momentum, $\vec{p}_{crystal} = \hbar\vec{k}$, where \vec{k} is the wave vector of the electron and set by the wavefunction in the crystal lattice [17]. When the maximum valence band energy and the minimum conduction band energy have the same crystal momentum, it known as a direct bandgap. Indirect bandgaps exist when these extrema occur for different

values of the crystal momentum. When an electron combines with a hole, momentum must be conserved along with energy. For an indirect bandgap, a transition from the conduction to valence band requires a change in the momentum of the electron which is large compared to momentum of an individual photon, $p = h/\lambda$. For indirect bandgap materials, radiative transitions between the conduction and valence bands are therefore highly unlikely, as energy and momentum are usually conserved by the emission of phonons, which have a much larger momentum, not photons. Because we want our laser diode to emit many photons, the semiconductors used in laser diodes is restricted to only ones with a direct bandgap, which severely limits the choices of semiconductors which can be used to create laser diodes, and it rules out popular semiconductors like silicon. The frequency of light produced in the transition between the conduction band and valence band is found using

$$E_B = hf. \quad (2.11)$$

For the bandgap structure, the probability of finding an electron in the conduction band and is given by the Fermi-Dirac distribution,

$$f_c(E_c) = \frac{1}{e^{(E_c - E_f)/k_B T} + 1}, \quad (2.12)$$

where E_c is the conduction band energy and E_f is the Fermi level. The 470 nm laser diode used has a bandgap of around 2.6 eV, implying that at room temperature, the vast majority of the electrons are in the valence band. The bandgap of semiconductors is large compared to metals, which have a much

greater number of electrons in the conduction band and explains the larger conductivity compared to semiconductors. Because the majority of electrons are in the valence band, this will eventually show the need for a pumping mechanism to get electrons into the conduction band so they can radiatively transition from the conduction band to the valence band. The distribution is temperature dependent, which in turn has effects on the bandgap energy and the frequency of an emitted photon. This also shows the need for laser diodes need to be temperature stabilized in order to operate at a constant frequency.

There are three primary radiative processes to consider to show the amplification properties of lasers [14]. These processes can occur in atoms and molecules, but I'll discuss them in terms of the bandgap structure found in a semiconductor. The first is absorption, where an incident photon with energy greater than the bandgap energy can promote an electron from the valence band to the conduction band. The reverse process is spontaneous emission, in which a photon is emitted as an electron transitions from the conduction band to the valence band. The energy of the photon will be equivalent to the bandgap energy, but will be emitted in a random direction and with a random phase. The emission of a photon may be stimulated as well, in which an applied electric field can perturb an electron in the conduction band to transition to the valence band, in the process producing a photon which is coherent (has the same phase relationships with each other).

The Einstein A and B coefficients give the rate at which these processes occur for a given system. A_{cv} is the coefficient for determining spontaneous emission, for B_{cv} is stimulated emission, and B_{vc} is absorption (and $B_{cv} = B_{vc}$).

These are set by the atomic structure, and can be calculated, but are often determined experimentally. We can look at the movement of electrons in our semiconductor. For N_c electrons in the conduction band and N_v electrons in the valence band, with $\rho(\omega)$ being the intensity of the light field at a particular frequency, the rate of change in the number of electrons in the conduction band is given by

$$\frac{dN_c}{dt} = -A_{cv}N_c - B_{cv}N_c\rho(\omega) + B_{vc}N_v\rho(\omega). \quad (2.13)$$

To amplify a beam passing through the system, the number of photons exiting must be greater than the number into the system. Therefore, the number of emissions must be greater than the number of absorptions. We can observe that if a large number of electrons are in the valence band, there will be many available electrons to absorb photons and the beam will be attenuated. As the number of electrons in the valence band decreases (and the number in the conduction band increases), not only are there fewer electrons to absorb photons, but the number of stimulated emissions will increase.

This condition at which we get amplification is called the threshold condition, and it requires a population inversion, where more electrons are in the higher energy state than the lower energy state. From Eq. 2.12, the majority of the electrons will be in the valence band around room temperature and materials with a bandgap suitable for emission at optical frequencies. A pumping mechanism is therefore required to get more electrons in the conduction band than the valence band. For a diode laser, this is accomplished by injecting

electrons into the n -doped side.

The region of the semiconductor structure which produces radiation is called the active region. In laser diodes, it is typically long rectangular prism, with the electrodes placed on top and bottom for current injection. The active region serves as a waveguide, and manufacturing techniques such as modifying the index of refraction or the gain of the semiconductor surrounding the active region are employed to confine the light to only the active region. Light exits the active region out the side of the semiconductor. Both faces are manufactured so they reflect the beam, forming the optical cavity inside the semiconductor. The height of the active region is typically limited by the desire to create a low threshold current for laser action, which is dependent on the injection current density [16]. This leads to the emission of an astigmatic beam due to the different divergences in the vertical and horizontal directions. The astigmatism can be corrected for using cylindrical lenses outside of the laser (Section 3.2).

2.2.2 External Cavity Diode Lasers

An external cavity diode laser uses a laser diode as the gain medium in an optical resonator outside of the semiconductor. The wavelength range of an ECDLs are therefore limited to the range of available laser diode wavelengths. While in recent years the range of wavelengths covered by laser diodes has increased greatly, making a suitable laser diode in the UV is difficult to engineer, and there are currently no commercially available 235nm ECDL's [14]. While many laser diodes are used without an external cavity, this design presents a

number of limitations including a broad emission linewidth and large mode hops. These limitations motivated the development of the ECDL, where the laser diode typically has a reflective coating on one face and an anti-reflection coating at the other end. The reflective end of the diode forms one edge of an optical cavity, while the other edge is typically bounded by a diffraction grating. The diffraction grating is angled so the first order reflection of only the desired wavelength is reflected back towards the laser diode. This amplifies only a narrow frequency range, reducing the linewidth of the emitted radiation, and also enables the laser frequency to be tuned without adjusting the temperature of the laser diode. The grating is usually placed on a piezoelectric actuator so that the length of the optical cavity can be continuously adjusted. By controlling both of these mechanisms in tandem, the resonant frequency can be adjusted, allowing for operation across a range of frequencies. Combined with the narrow linewidth, ECDL's are useful for tuning onto a spectral line of an atom or molecule.

The frequency the ECDL will lase at is determined by the frequency with the largest overall gain. This is determined gain profile of the laser diode, the laser diode cavity, and resonant mode of the external cavity. The broad frequency tuning in an ECDL is controlled by varying the gain of the laser diode. The Gallium Nitride (GaN) laser diode used in our experiment has a measured peak gain at 471.9 nm, but will also lase down to 468.8 nm and up to 476.3 nm [18]. This is controlled by large adjustments to the diode temperature and current, which modifies the bandgap. For finer frequency tuning, the angle of the diffraction grating and the length of the external cavity are adjusted in

tandem to control the resonant frequency of the external cavity. The finest and quickest frequency tuning comes from small adjustments in the current.

One notable behavior and limitation in tuning the frequency of an ECDL is mode hopping, where the frequency of the laser experiences a large jump. As the external cavity resonant frequency moves relative to the gain of the laser, there comes a point where that cavity mode no longer has the largest overall gain, and the frequency of the laser hops as the laser switches from lasing at one mode to another. A simplified picture of this behavior is illustrated in Fig. 2.1. Our ECDL has a mode hop free tuning range of 23 GHz, which should allow for us to tune the frequency to hit the $2s$ to $2p$ resonant frequency of the beryllium atom.

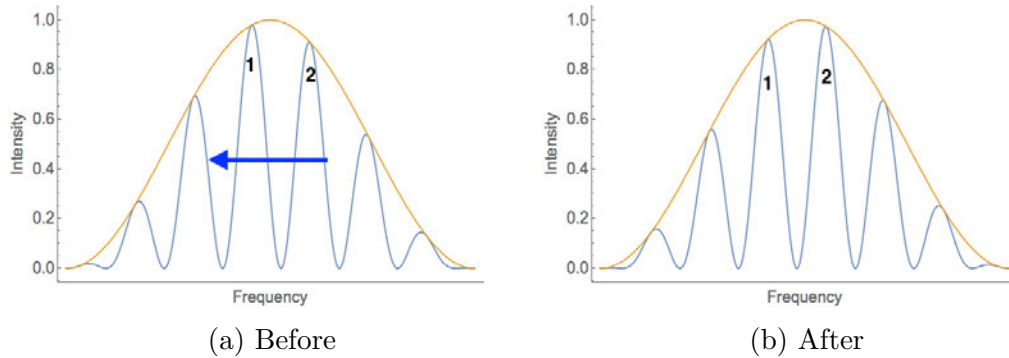


Figure 2.1: An external cavity diode laser, lasing at the frequency designated by (1) in 2.1a, switches to mode 2 in 2.1b as the external cavity mode (blue) drifts relative to the laser diode gain (orange). Once (1) surpasses (2) in amplitude, the laser starts lasing at the frequency of mode (2), causing a hop in the emitted frequency.

2.3 Second Harmonic Generation

The polarization of the electric field in a material is typically approximated as being linear

$$P = \chi E(t)\epsilon_0, \quad (2.14)$$

where χ is the electric susceptibility of a particular material. For small intensities of light and for most materials, this is a fine approximation. However, with higher intensities, and therefore larger electric fields, to accurately model the polarization in a material, higher order terms are needed:

$$P(t) = \chi_1 E(t)\epsilon_0 + \chi_2 E^2(t)\epsilon_0 + \chi_3 E^3(t)\epsilon_0 + \dots \quad (2.15)$$

For some materials, the electric susceptibility coefficients higher order terms are substantial, and are large enough where significant nonlinear polarization terms appear. These special “nonlinear” materials can be used to produce frequencies of light which are different than the incident light. In second harmonic generation, light at double the original (fundamental) frequency is produced. Nonlinear effects are most often observed in crystals, where the repeatable structure allows for the higher order susceptibility terms to be larger.

The origin of the higher order electric susceptibility terms can be observed by using the Lorentz model of the atom, which approximates the electron as a mass on a spring connected to a much larger nucleus [19]. For small displacements from its equilibrium position (small electric fields), the response of the electron is to move at a frequency of the applied field. This assumes

the electromagnetic wave is at the resonant frequency of the the potential. To describe the fact the crystal does not have only specific resonances that can be doubled, a model using quantum mechanics is needed [19]. If we allow the displacements to be larger and introduce terms which make the potentials anharmonic, the motion of the electron can be described by a series, with each term in the series corresponding to a harmonic of the applied field. If the potential is asymmetric, corresponding to a non-centrosymmetric crystal (where there is no inversion symmetry, or the crystal structure is not identical for every set of points (x, y, z) and $(-x, -y, -z)$), then the series which corresponds to the equation of motion of the electron in the potential has a component at the fundamental frequency as well as the second harmonic (and additional higher harmonics). The asymmetry is crucial to creating a non-zero second order electric susceptibility term (χ_2) which is responsible for second harmonic generation. The changes to the potential energy function for an electron in a crystalline structure comes from interactions between the electrons and the surrounding positively charged nuclei.

The presence of an electromagnetic wave created at twice the frequency of the fundamental can be shown by supposing an incident plane wave of frequency ω is incident on the material, and the electric field at a chosen point is

$$E(t) = E_0 e^{-i\omega t} + E_0^* e^{i\omega t}. \quad (2.16)$$

Examining how the power series representation of the polarization (Eq. 2.15)

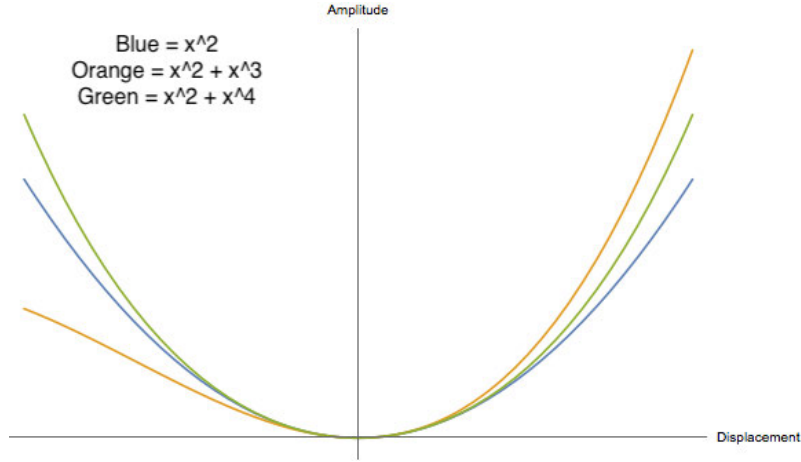


Figure 2.2: Sample potentials representative of a linear material (blue), a non-centrosymmetric crystal (orange), and a centrosymmetric crystal (green). For small displacements (low electric field intensities), each potential resembles the linear material.

will respond, the second order term will be

$$P_2(t) = \chi_2 |E(t)|^2 \epsilon_0 = 2\chi_2 E E^* \epsilon_0 + \chi_2 E^2 e^{2i\omega t} \epsilon_0 + \chi_2 (E^*)^2 e^{-2i\omega t} \epsilon_0, \quad (2.17)$$

which indicates the polarization has a component which depends on twice the frequency of the incident wave. The second order polarization term only occurs in materials lacking inversion symmetry (like in a non-centrosymmetric crystal) [19], where inversion symmetry specifies that for a given axis, the crystal lattice at point (x, y, z) is identical at $(-x, -y, -z)$. The polarization term $P_2(t)$ oscillates at twice in the input frequency, in addition to $P_1(t)$, which oscillates at the fundamental frequency. From Faraday's Law and Ampere's

Law in matter without any local charge,

$$\nabla \times \vec{H}(t) = \frac{\partial}{\partial t}(\epsilon_0 \vec{E}(t) + \vec{P}(t)) \quad (2.18)$$

$$\nabla \times \vec{E}(t) = -\frac{\partial}{\partial t}(\mu_0 \vec{H}(t)), \quad (2.19)$$

the changing polarization is responsible for creating a changing $\vec{H}(t)$ in the material, which in turn is responsible for creating changing $\vec{E}(t)$, producing electromagnetic waves in the material. One part of the polarization will oscillate at the fundamental frequency, while the other oscillates at twice the fundamental, producing two waves, one with frequency ω , and the other with frequency 2ω .

To find the intensity of the second harmonic beam produced, the stength of the interaction in the material is usually given by the effective nonlinear coefficient, d_{eff} instead of a higher order polarization term. d_{eff} is found by multiplying the nonlinear optical susceptibility tensor by the crystal axis along which the incident wave is polarized. The nonlinear optical susceptibility tensor gives the nonlinear polarizations in terms of the crystal axes, with the geometry of the crystal defining the non-zero terms. The total intensity of the second harmonic is calculated by finding the electric field amplitude at the second harmonic in a infintesimally small width of the crystal and then integrating over the length of the crystal, which gives [14]

$$I^{(2\omega)} = \frac{1}{2} \left(\frac{\mu_0}{\epsilon_0} \right)^{3/2} \frac{\omega^2 (d_{\text{eff}})^2 L^2}{n^3} (I^{(\omega)})^2 \frac{\sin^2(\Delta \vec{k} L/2)}{(\Delta \vec{k} L/2)^2}, \quad (2.20)$$

where $I^{(\omega)}$ is the intensity of the fundamental, and L is the length of the crystal. The final term takes into consideration the phase matching between the fundamental and second harmonic, discussed in Section 2.4.1. Notably, the power of the second harmonic generated is proportional to the square of the power of the fundamental beam.

2.4 Optimal Second Harmonic Generation in Beta Barium Borate

For producing light at 235 nm by second harmonic generation, Beta Barium Borate (BBO) is the crystal of choice. While other crystals are either damaged by ultraviolet light or are not transparent at these short wavelengths, BBO has a wide window of transparency which contains our desired frequency (down to 198 nm), and thus is suitable for generating 235 nm light [14]. BBO is non-centrosymmetric (lacks inversion symmetry), and therefore supports second harmonic generation. Type 1 second harmonic generation is employed, where two photons at the fundamental frequency with ordinary polarization are converted to a single photon at the second harmonic with extraordinary polarization (detailed further in Section 2.4.1). For maximum UV output, the crystal must be cut so the fundamental and second harmonic are phase matched, where the fundamental and second harmonic remain in phase. Optimizing the focus of the fundamental, which for BBO includes accounting for the increasing spatial separation between the fundamental and second harmonic through the crystal, also known as walkoff. For accurately modeling the

second harmonic generation output, factors such as absorption in the material and reflection off the crystal face must be accounted for as well.

One of the design choices made to minimize the cavity transmission losses, which will be shown to maximize the resonator circulating power, is to cut the crystal faces at Brewster's angle to minimize the reflection off the input and output faces. Brewster's angle is calculated from

$$\theta_b = \arctan\left(\frac{n_2}{n_1}\right), \quad (2.21)$$

which for BBO is 59.25° . To take advantage of this cut, the light incident on the crystal must be horizontally polarized so it is in the plane of incidence of the crystal faces. Because the polarization of the second harmonic will be vertically polarized, the crystal-to-air interface is not at Brewster's angle for the 235 nm light, so about 23% of this light is reflected.

2.4.1 Birefringent Phase Matching in BBO

Dispersion leads to the fundamental and second harmonic shifting out of phase as they propagate through the crystal. Therefore, as the fundamental interacts with the crystal to produce more light at the second harmonic, the newly generated second harmonic will be out of phase with the existing second harmonic. To produce the maximum amount of radiation at the second harmonic, the fundamental and second harmonic must be kept in phase with each other to minimize destructive interference between the two [14]. From Eq. 2.20, the

second harmonic intensity is maximized when the term

$$\left(\frac{\sin(\Delta\vec{k}L/2)}{\Delta\vec{k}L/2} \right) \quad (2.22)$$

is equal to one, which is when the phase matching condition is met:

$$\Delta\vec{k} = 0 \rightarrow \vec{k}_2 = 2\vec{k}_1, \quad (2.23)$$

where \vec{k}_1 and \vec{k}_2 are the wavenumbers for the fundamental and SHG light respectively.

One solution is to make the crystal medium very short. After a distance of $\pi/\Delta\vec{k}$, named the coherence length and given by

$$l_c = \frac{\lambda}{4(n_{2\omega} - n_\omega)}, \quad (2.24)$$

the two beams will begin to be considerably out of phase. Solving for this length in the context of our experiment, with a BBO crystal with a fundamental of 470 nm, and the indices of refraction given by the Sellmeier Equation, this is the order of a few microns. Examining Eq. 2.20, the power of the second harmonic increases with the length of the crystal. Shortening the crystal is therefore not an attractive solution for phase matching.

A solution which allows for longer nonlinear media to be used is birefringent phase matching [14]. Birefringent materials, such as BBO, have an index of refraction which is a function of the direction of beam propagation in the material and its polarization. Therefore, the index of refraction for a beam

through the crystal depends on its wavelength, polarization, and direction. The second harmonic will have a polarization orthogonal to the fundamental, so one can adjust the direction of propagation so that the index of refraction for the fundamental and second harmonic are equal.

A propagation direction that has a index of refraction which is independent of the polarization is called an optical axis. Light polarized perpendicular to the plane defined by \vec{k} and the optical axis are called ordinary rays, and experience an index of refraction n_o , while light with polarization in the plane defined by \vec{k} and the optical axis are referred to as an extraordinary ray, and experiences a variable index of refraction, n_e , based on the direction. BBO is an uniaxial crystal (has a single optical axis), and more specifically, it is a negative uniaxial crystal, which means a set of two directions have an equal indexes of refraction which are larger than the index of refraction of the third (the z -axis will be used as the one with a different index of refraction, so $n_z < n_x = n_y$).

In a uniaxial crystal, as the angle of propagation is changed with respect to the optical axis, the index of refraction for one polarization will remain constant (the ordinary polarization), and change for the other (the extraordinary polarization). By specifying the direction of polarization for the fundamental, an angle can be found relative to optical axis so that the index of refraction for waves at the fundamental frequency and the second harmonic can be set equal to each other. Because BBO is a negative uniaxial crystal, the fundamental will be an ordinary beam and the second harmonic will be an extraordinary beam so that the larger dispersion is compensated by the lower index of re-

fraction for an extraordinary beam.

2.4.2 Optimal Focusing and Walkoff in BBO

Focusing the light through the crystal can improve second harmonic generation production. The more tightly focused the beam is, the larger the intensity of the fundamental will be near the focus, and because SHG production increases quadratically with the intensity of the fundamental (Eq. 2.20), more SHG light will be generated. The trade off is a smaller focus leads to a more rapidly diverging beam, and away from the focus the electric field strength will decrease rapidly. The strength of the focusing is characterized by the focusing parameter ξ , which is given in terms of the Rayleigh range and crystal length as

$$\xi = \frac{l}{2z_R}, \quad (2.25)$$

where the Rayleigh range is related to the waist size by Eq. 2.5. The optimal focusing parameter has been shown to be around 2.8 for second harmonic generation without walkoff [20]. In BBO crystals, another factor for determining optimal focusing parameter is the walkoff between the fundamental and second harmonic. Walkoff is due to the direction of the electromagnetic wave propagation given by \hat{k} , and the direction of energy in the wave given by the Poynting Vector (\hat{S}) being in different directions. The walkoff angle is given by

$$\tan \rho = \frac{1}{2}(n_{o,\omega})^2 \left(\frac{1}{(n_{e,2\omega})^2 - (n_{o,2\omega})^2} \right) \sin 2\theta, \quad (2.26)$$

where ρ and θ are the angle between the \vec{S} and \vec{k} respectively to the optical axis. For the large walkoff in BBO, it has been shown that the focusing must be much weaker (around 1.4) than for cases where there is little to no walkoff to achieve optimal focusing [20] The focusing parameter needs to be much less, which implies a larger Rayleigh range, so therefore a larger waist. While the walkoff parameter must be taken into consideration to determine the optimal focusing, it can lead to a serious loss of power at the second harmonic. For large walkoffs, the asymptotic behavior of the second harmonic power goes increases with the square root of the length of the crystal, as opposed to linearly with the crystal length for no walkoff [14].

2.5 Optical Resonators

The power of the second harmonic produced is proportional to the electric field intensity squared, so in order to increase the efficiency of the conversion, an optical resonator was built around the crystal to increase the power through the crystal. The resonator is designed to maximize the conversion between the fundamental and second harmonic and produce a single beam with the largest intensity possible. The resonator design of choice is a ring cavity in a symmetric bowtie configuration. This setup has many advantage over a Fabry-Perot cavity for second harmonic generation. In a Fabry-Perot cavity, additional complications are added because the beam at the fundamental frequency (pump beam) passes through the nonlinear media in both directions. This means that two beams at the higher harmonic will be cre-

ated, but they will have a smaller amplitude. Both mirrors must also be coated so they are transparent at the second harmonic. In a bowtie configuration, the pump beam passes through an input coupler, which has a chosen transparency at the fundamental wavelength to match the other losses as it circulates around the cavity (see Section 2.5.2). The beam is then incident on a mirror connected to a piezoelectric actuator. The light reflected off of the mirror attached to the piezo stack is incident on a curved mirror to focus the light down to the appropriate waist inside the crystal. The beam emerges from the crystal and is incident on the output coupler, which is coated to be highly reflective at the fundamental frequency, and has been measured to only allow 0.125% of 470 nm through, but transparent at the second harmonic, and transmits 0.095% of 235 nm light. The output coupler has an identical radius of curvature to the previous mirror.

For the cavity to be stable and on resonance, the wave must replicate itself each pass around the cavity. For this to happen, two conditions must be met. If we select an arbitrary point along the beampath in the cavity, the phase of the light must be a multiple of 2π so each subsequent pass interferes constructively. The field amplitude distribution must replicate itself after each pass around the cavity as well. To analyze the properties of the cavity, we can write down the ABCD matrix for a round trip around the cavity. The ABCD matrix allows for a simple calculation of the transformation of the complex beam parameter as it reflects off a mirror, is focused by a lens, or passes through different media, which the interaction between each element represented by matrix multiplication [14]. For an initial complex beam parameter

q_0 , calculation of the ABCD matrix yields a new complex beam parameter:

$$q_1 = \frac{Aq_0 + B}{Cq_0 + D}, \quad (2.27)$$

so for the cavity to be stable, after a pass around the cavity, $q_0 = q_1$. The calculation of the ABCD matrix for a ring cavity, and neglecting astigmatism, is given by

$$\begin{bmatrix} A & B \\ C & D \end{bmatrix} = \begin{bmatrix} 1 & 0 \\ -\frac{2}{R} & 1 \end{bmatrix} \begin{bmatrix} 1 & R(1-g_1) \\ 0 & 1 \end{bmatrix} \begin{bmatrix} 1 & 0 \\ -\frac{2}{R} & 1 \end{bmatrix} \begin{bmatrix} 1 & R(1-g_2) \\ 0 & 1 \end{bmatrix}, \quad (2.28)$$

which results in

$$\begin{bmatrix} 2g_1 - 1 & R(-2g_1g_2 + g_1 + g_2) \\ \frac{-4g_1}{R} & 4g_1g_2 - 2g_1 - 1 \end{bmatrix} \quad (2.29)$$

where two dimensionless parameters have been used, defined as

$$g_1 = 1 - \frac{d_1 + 2d_2}{R}, g_2 = 1 - \frac{d_3}{R} \quad (2.30)$$

and refer to the distances are shown in Fig. 2.3, while R is the radius of curvature of the mirrors. There is necessarily an astigmatism that is introduced when the beam reflects off the curved surface of the mirror. We compensate for this astigmatism using the off-axis transmission through the crystal, which also introduces an astigmatism [14].

In terms of the ABCD matrices, each trip around the cavity is like multiplying by the result of Eq. 2.29. For n trips around the cavity, the resulting

matrix can be evaluated using Sylvester's Theorem, where

$$\begin{bmatrix} A & B \\ C & D \end{bmatrix}^n = \frac{1}{\sin \theta} \begin{bmatrix} A \sin n\theta - \sin(n-1)\theta & B \sin n\theta \\ C \sin n\theta & D \sin n\theta - \sin(n-1)\theta \end{bmatrix}, \quad (2.31)$$

where solving for θ yields

$$\theta = \cos^{-1}\left(\frac{1}{2}(A + D)\right), \quad (2.32)$$

so for θ to be real,

$$|A + D| \leq 2, \quad (2.33)$$

which is called the stability criterion. In terms of g_1 and g_2 , the stability criterion is

$$0 \leq g_1 g_2 \leq 1. \quad (2.34)$$

Two beam waists are formed: one along the long arm between the two plane mirrors, and one in between the curved mirrors. The waist between the curved mirrors for SHG is more important, because by optimizing this waist, the second harmonic conversion is optimized. The waist radius between the curved mirrors is given by

$$\omega_0^2 = \frac{\lambda R \sqrt{g_1 g_2 (1 - g_1 g_2)}}{2n\pi g_1}, \quad (2.35)$$

and the waist radius between the planar mirrors is

$$\omega_0'^2 = \frac{\lambda R \sqrt{g_1 g_2 (1 - g_1 g_2)}}{2n\pi g_2}, \quad (2.36)$$

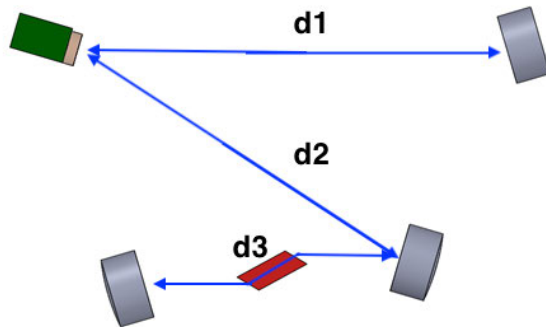


Figure 2.3: Symmetric bowtie cavity and illustrations of lengths used in calculating cavity parameters. d_3 includes the length of the crystal, adjusted for the index of refraction.

which determines the waist needed for mode matching light from the laser into the cavity (see Section 3.2). The resonant frequency of the cavity is given by

$$\nu_{nmq} = \left(q + (n + m + 1) \frac{\cos^{-1} \sqrt{g_1 g_2}}{\pi} \right) \frac{c}{L}, \quad (2.37)$$

where n and m are the mode numbers for the Hermite-Gaussian modes, and q is the axial mode number. Different modes therefore have different resonant frequencies, which is consistent with the change in the phase evolution given by Eq. 2.3.

2.5.1 Power Enhancement

Determining the energy relationships inside the cavity will be used to calculate the second harmonic power generation. The reflected beam off the input

coupler will also be used for determining how much power is circulating in the cavity and will be monitored in order to lock the cavity (See Section 4.3). At the surface of a mirror, a percentage R of the light is reflected, while a percentage T is transmitted through the mirror, with $T + R = 1$. For simplicity, the transmission and reflection of the mirrors apart from the input coupler can be lumped into a single term, designated R_A and T_A . There are other variable sources of attenuation of the beam as it propagates between the mirrors, most notably from the second harmonic generation through the crystal, which is given this the transmission coefficient T_0 . Because the field strength and intensity are related quadratically, the amplitude coefficients are given as lowercase, while power coefficients are uppercase, so that

$$T_0 = t_0^2, R_0 = r_0^2. \quad (2.38)$$

For a beam with initial electric field strength E_0 , at the input coupler transmits a field of

$$t_1 E_0 \quad (2.39)$$

and reflects

$$r_1 E_0. \quad (2.40)$$

Including losses propagating through the cavity, a single pass around the cavity can be modeled by

$$t_0 r_A r_1, \quad (2.41)$$

where t_0 is the amplitude transmission coefficient of the cavity, while r_A is

the combined amplitude reflection coefficients of the mirrors. After adding this pass around the cavity to the input beam, the electric field at the input coupler is

$$E_0 t_1 + E_0 t_1 t_0 r_A r_1, \quad (2.42)$$

where the fields can be summed together due to superposition. If we keep summing passes around the cavity, this yields a circulating electric field strength of

$$E_c = E_0 t_1 + E_0 t_1 t_0 r_A r_1 e^{-i\delta} + E_0 t_1 t_0^2 r_A^2 r_1^2 e^{-2i\delta} + \dots, \quad (2.43)$$

where the term $e^{-i\delta}$ has been added to account for if the passes are in phase with each other, with δ corresponding to the round trip phase shift. The total circulating field strength can be found by summing all the passes through the cavity. The terms form a geometric series, and the result is [14]:

$$E_c = E_0 \frac{t_1}{1 - r_1 r_A t_0 e^{-i\delta}}. \quad (2.44)$$

The circulating power on resonance is therefore

$$I_c = I_0 \frac{t_1^2}{(1 - r_1 t_0 r_A)^2}, \quad (2.45)$$

where I_0 is the intensity of the input beam. Taking the example of a 99% input coupler, with a 100 mW input beam, and a collective loss of 1% between the remaining mirrors and propagation through the cavity, the circulating power is 10 W, providing power enhancement factor of 100. From Eq. 2.20, we can see this provides a factor of 10,000 increase in the amount of second

harmonic power that could be created. The behavior of the real system is less than this, because the round trip losses increase at higher powers because the fundamental is depleted due to the high conversion to the second harmonic.

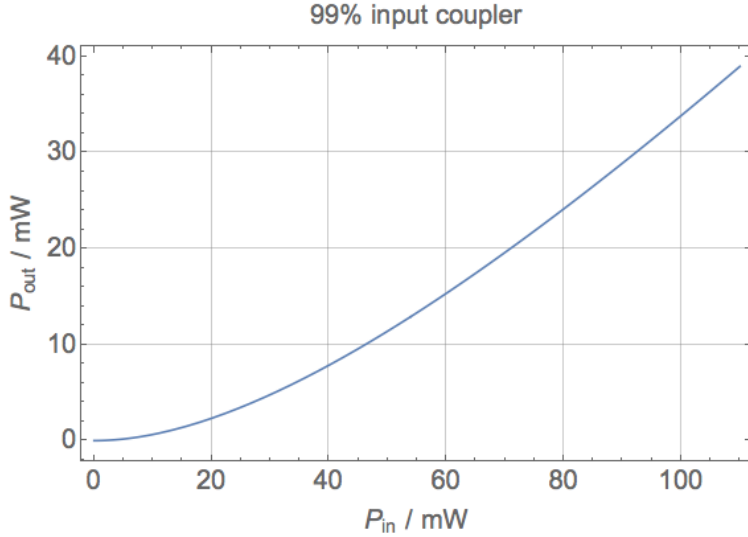


Figure 2.4: Second harmonic generation output power vs input power including Brewster losses for our cavity with optimal SHG and impedance matching with a 99% input coupler. At large input powers, the gain in the second harmonic output becomes linear as the loss of the fundamental becomes significant.

Examining the reflected beam, the electric field of the reflected beam which reflects off the input coupler and never enters the cavity is $E_0 r_1$. Like the internal field, the reflected field can be found by summing over the transmission through the input coupler of each pass around the cavity. Each pass contributes

$$E_0 t_0^2 r_A r_1 e^{-i\delta}, \quad (2.46)$$

to the reflected field. Summing over all the passes yields an electric field of [14]

$$E_r = E_0 \frac{r_A t_0^2 e^{-i\delta} - r_1}{1 - r_1 r_2 t_0^2 e^{-i\delta}}, \quad (2.47)$$

and the intensity is

$$I_c = I_0 \frac{(r_1 - r_A t_1)^2 + 4r_1 r_A t_1 \sin^2 \delta/2}{(1 - r_1 r_A)^2 + 4r_1 r_m \sin^2 \delta/2}. \quad (2.48)$$

2.5.2 Impedance Matching

To maximize the circulating power in the cavity, the derivative of Eq. 2.48 shows that when the cavity is on resonance, there is a maximum when the transmission loss through the input coupler matches all of the other losses in the cavity, which is referred to as impedance matching. Figure 2.5 shows how the circulating intensity is maximized when the reflection coefficient of the input coupler matches the fraction of the electric field which remains after one trip, $r_m^2 = 1 - T_0 \times R_A$.

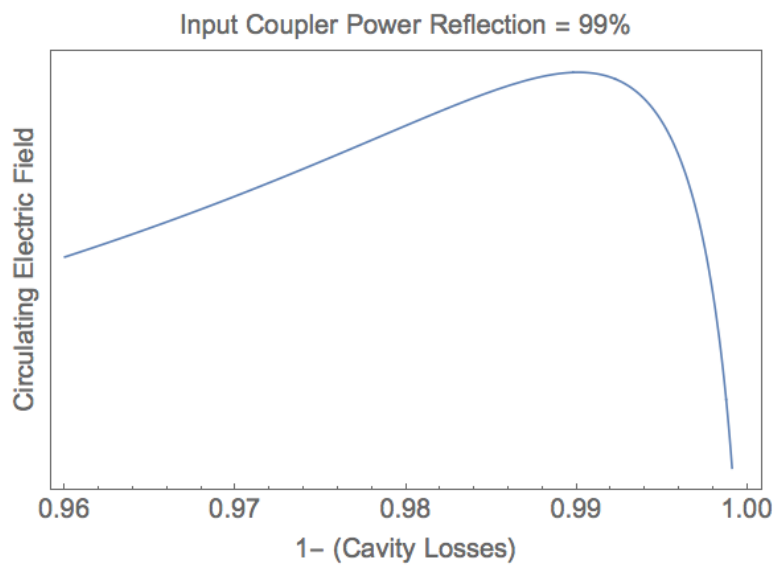


Figure 2.5: Circulating electric field versus choices for the coefficient of reflection for a 99% input coupler. Note the maximum occurs when the round trip cavity losses equal the transmission of the input coupler.

Chapter 3

Building and Optimizing the Cavity

This chapter will cover the steps taken to produce ultraviolet light, starting with the construction of the monolithic cavity, and continuing to include the design of the optics to couple the light into the cavity, and the experimental techniques used to detect and measure the output beam.

3.1 Monolithic Cavity Design in Solidworks

Once the optical resonator parameters were determined, a model of the cavity was made in SolidWorks. The mirror positions were set based on the resonator parameters. When all of the optical elements were inserted, the beam path (including beams entering or leaving the cavity) could be modeled. The mirror mounts (Thorlabs KS-05) were then added, which set the position of the cavity walls. The mirror mounts each have three degrees of freedom: one each for

vertical and horizontal adjustments of the beam, and a third for translating the mirror surface horizontally. The cavity was left open on one side to mount the crystal aligner (Newport 9081 Five-Axis Aligner), which allows for the crystal to be rotated and yawed, as well as translated side to side. A BNC connector is installed for the piezo, along with a spare for an additional device.

The blue light coupled into the cavity enters through the input coupler mirror (IC), which is coated on a single side with a carefully set reflectivity. The transmitted light is incident on a small mirror attached to a piezoelectric actuator which will length-stabilize the cavity against vibrations. A programmable FPGA servo controls the feedback voltage applied to the piezo. Light reflects off the small mirror onto a curved mirror, which focuses the beam into the BBO crystal. The input and output crystal faces are cut at Brewster's angle so there is minimal attenuation of the 470 nm light at the interfaces. Because the polarization of the second harmonic is polarized vertically, some of this light will reflect off the crystal face. The cavity has a window designed to allow this 235 nm light to pass out of the cavity. The 235 nm light which exits the crystal face will be incident on the output coupler mirror. The coating applied to this mirror makes it highly transmissive at 235 nm. The 470 nm light reflects off the output coupler, where it is directed back at the input coupler and comes to a large focus along the long arm. Further design details are included in Appendix A. This design was inspired by Ref. [13].

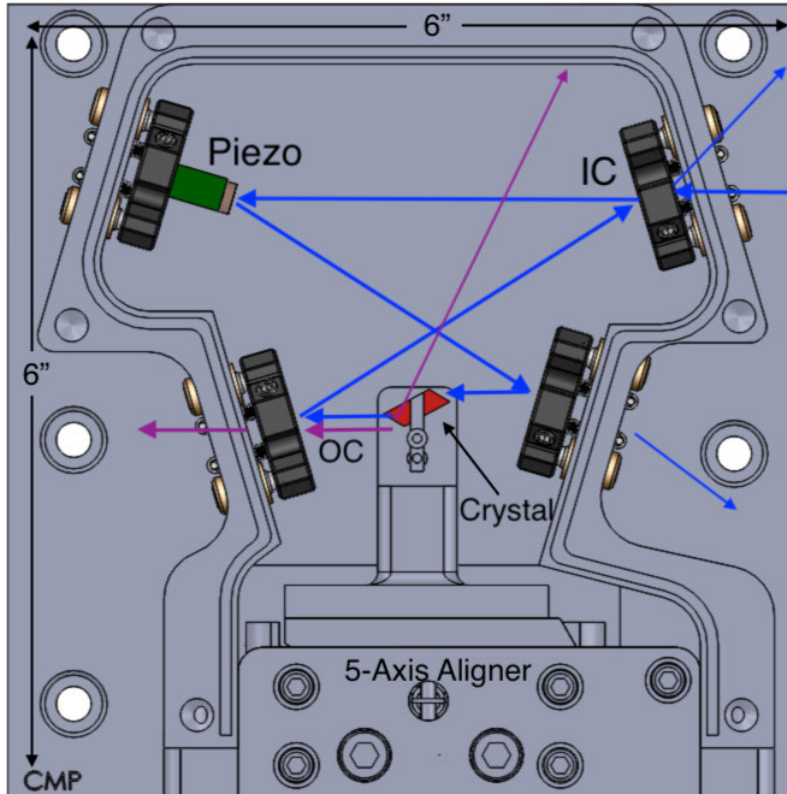


Figure 3.1: Solidworks rendering of the cavity design, including the path the 470 nm light takes (blue) and the path of the 235 nm light (violet).

3.2 Input Optics

The beam out of the laser must be mode matched to the resonant mode of the cavity. This entails focusing the input beam to the correct shape and position so that only the lowest order transverse Gaussian mode (Eq. 2.4) is resonant in the cavity. The beam must be horizontally polarized so the reflection off the crystal face is minimized due to the Brewster cut of the crystal. Additionally, the birefringent phase matching of the fundamental and second harmonics requires the input beam be horizontally polarized. The entire optics setup,

including cavity and laser head, is mounted to an 18" x 18" optical breadboard. The breadboard provides another stage of passive dampening from vibrations, and allows the setup to be moved without realigning the optics. Figure 3.2 shows the main optical elements, and the remainder of this section describes their function.

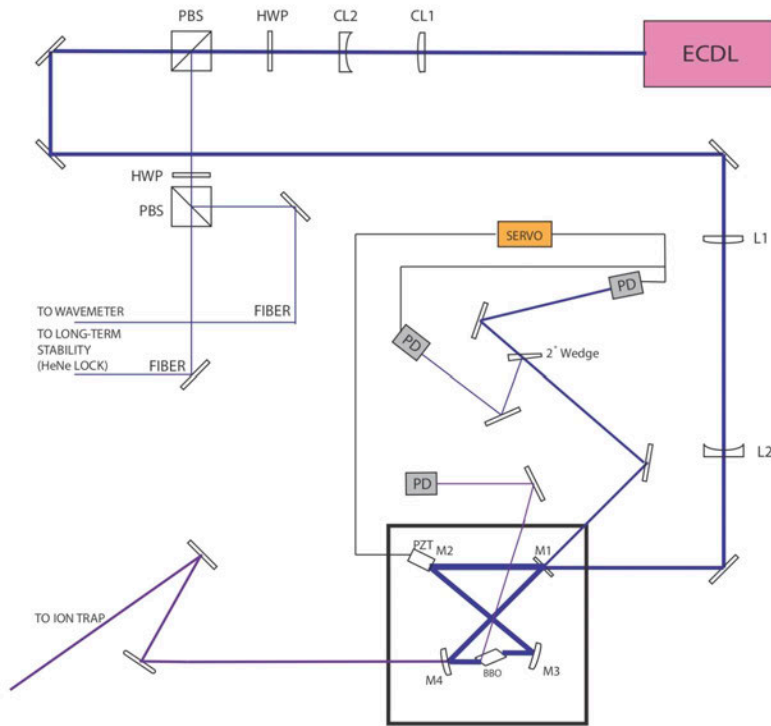


Figure 3.2: Beryllium Photoionization Laser System. Blue light from the ECDL is coupled into the power enhancement cavity to increase the amount of UV light produced by second harmonic generation. The elements which make up the feedback control system are detailed in Section 4.3.

Due to the rectangular shape of the active region of the laser diode, the output beam of the ECDL is astigmatic. To circularize and collimate the beam, the shape of the original beam was measured using a CCD sensor and

software which calculated the horizontal and vertical beam spot sizes. Two cylindrical lenses were inserted into the beam path to circularize the output: a 100mm focal length plano-convex cylindrical lens and a -50mm focal length plano-concave lens. Together, they form a Galilean telescope which squeezes the width of the beam to approximately the same size as the height. After passing through the cylindrical lens arrangement, the beam has a 1.23 width to height ratio, as opposed to an original 2.27 width to height ratio. The beam at this point is collimated, and measurements of the spot size at different distances from the laser aperture yield a divergence which is consistent with the Rayleigh range of the beam.

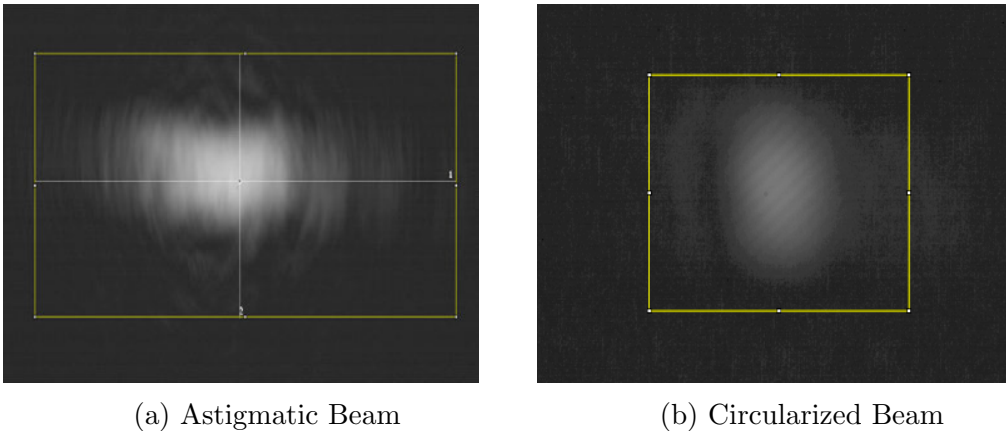


Figure 3.3: Beam shape before (a) and after (b) passing through cylindrical lenses. The resulting beam has a 2.1 mm horizontal waist and 1.7 mm vertical waist after passing through the cylindrical lenses.

The majority of the beam will be coupled into the resonator. Part of the beam is picked off so that the wavelength can be monitored and stabilized (see Section 4.4). To accomplish this, a half-waveplate rotates the beam polarization before entering a polarizing beamsplitter. The half-waveplate is held

in a rotational mount so the polarization of input beam can be rotated, and therefore adjust the amount of light which is picked off. The polarizing beam-splitter is transparent to horizontally polarized light, while vertically polarized light is reflected 90° so only horizontally polarized light enters the cavity.

The light directed into the cavity must be matched to the resonant mode of the cavity. The matching involves bringing the input beam to a focus at the same position and size as the large cavity waist. Two mirrors steer the beam through a set of two lenses (L1 and L2 in Figure 3.2) which focus the beam. This can be done with a single lens, but it requires the exact choice of focal length to be available, as the size and position of the waist will both be set by the focal length of the lens. A two lens system provides an additional degree of freedom, and combinations of readily available lenses can be chosen to match the resonant mode of the cavity. Adjusting the distance between the two lenses and the distance from the lenses to the desired focal point allows for adjustments to be made to the size and position of the waist [14].

After the cylindrical lenses, the beam propagates a distance d_1 , then passes through a lens with focal length f_1 . It then propagates a distance d_3 between the first and second lenses, which has a focal length of f_2 . This can be modeled with the following ABCD matrix:

$$\begin{bmatrix} A & B \\ C & D \end{bmatrix} = \begin{bmatrix} 1 & 0 \\ -1/f_2 & 1 \end{bmatrix} \begin{bmatrix} 1 & d_3 \\ 0 & 1 \end{bmatrix} \begin{bmatrix} 1 & 0 \\ -1/f_1 & 1 \end{bmatrix} \begin{bmatrix} 1 & d_1 \\ 0 & 1 \end{bmatrix}. \quad (3.1)$$

The transformation of the complex beam parameter after traveling a length

d_2 after the second lens is

$$q_2 = \frac{Aq_1 + B}{Cq_1 + D} + d_2. \quad (3.2)$$

By using Eq. 2.8 and solving for when the lens separation d_3 yields a radius of curvature of infinity, the waist of the beam can be calculated at the desired focus point with Eq. 2.10. A Mathematica notebook was developed to solve for the proper lens separation. The focal lengths of the lenses are constrained by the available lenses and the physical layout of the input optics and cavity. Further, certain lens combinations yielded a small range of stable operation before not being able to focus the beam (for a given input spot size, a pair of lenses can only bring the output beam to a focus at a limited distance in space). d_2 was manually varied within the physical constraints of the input optics setup.

The optimal set of lenses were mounted in a cage mount system which allowed for their position to be easily adjusted during the coupling process. The second lens is mounted in an XY translation mount which provides two additional degrees of freedom for steering the beam through the input coupler and onto the piezo mirror. Light which reflects off the input coupler of the cavity is directed towards photodetectors, made with a printed circuit board. The photodetectors are part of a servo control system which will be used to lock the cavity on resonance (see Section 4.3).

3.3 Generating UV Light from a Single Pass

For optimal UV output, the fundamental beam must propagate through the crystal at the correct angle to satisfy the phase matching condition. The crystal is cut so that the fundamental and second harmonic are phase matched when propagating parallel to the long face of the crystal. The following method was used to initially position the crystal close to the optimal angle. Using the 5-axis aligner, the crystal was positioned so the beam traveled along the edge of the crystal. The crystal face provides a reference to ensure the beam is parallel to the long face of the crystal. The stage was then translated so the beam entered through the crystal center while preserving the angle at which the beam passed through the crystal. A similar procedure was used to ensure the “pitch” of the crystal was correct and it was going through the vertical center, using the top face of the crystal as the reference to ensure the correct angle.

Ultraviolet light produced by second harmonic generation in the crystal was first observed by steering light through the crystal with the input coupler of the optical resonator removed. The beam only makes a single pass through the crystal, which presents two advantages. First, before the mode matching and alignment of the cavity is optimized, the input coupler will reflect most of the input light, reducing the quantity of UV light produced. Additionally, it allows for the crystal angle to be optimized without adjusting the cavity alignment simultaneously. Adjusting the crystal angle in the resonant cavity changes the beam path, which requires adjusting the mirror mounts to walk back the spatial overlap of the passes. Adjusting the crystal angle also changes

the UV production efficiency. After optimizing the crystal alignment, it freezes many degrees of freedom, which reduces the complexity of coupling the light into the cavity. The drawback is the amount of UV light produced will be small because the incident power is only the 100 mW output of the laser (Eq. 2.20), so observing the UV light takes care.

Available photodiodes and other detection methods were sensitive to both the fundamental and second harmonic, which necessitated that the UV be separated from the blue. This was done by placing two extra output couplers, which are transparent at 235 nm but reflective at 470 nm, between the cavity output and the photodetector. Roughly 1 in 10^{10} blue photons will be transmitted through all three mirrors. The presence of UV could be seen by a paper index card fluorescing.

Another confirmation of UV light was by using a diffraction grating to spatially separate the two wavelengths. At a wavelength λ , the angle a normally incident beam reflects off the grating is given by

$$\theta_m = \arcsin\left(\frac{m\lambda}{d}\right), \quad (3.3)$$

where m is the order of the diffraction and d is the split spacing. For the 1800 lines/mm grating used, this corresponds to a diffraction from normal incidence at an angle of $\theta_1 = 25.3^\circ$ for 235 nm light and $\theta_1 = 58.7^\circ$ for 470 nm light. Spots were observed on an index card which matched the predicted diffraction angles.

The single pass maximum power output was measured to be $0.9 \mu\text{W}$ for a

100 mW input beam. This value was measured through the output coupler of the cavity, along with two additional output couplers, each which transmits only 95% of the UV light [21]. Taking into account the 22.7% reflection off the crystal face and the transmission of the three output couplers, the conversion efficiency in the crystal, again characterized by γ , is estimated to be

$$\gamma = \frac{P_{2\omega}}{P_{\omega}^2} = 1.35 \times 10^{-4} \text{ W}^{-1}, \quad (3.4)$$

which we can compare to the theoretical value of $\gamma_{calc} = 1.66 \times 10^{-4} \text{ W}^{-1}$, which is set by the effective nonlinear coefficient, wavelength of the fundamental, phase matching, walkoff, and focusing parameters.

3.4 Aligning the Cavity and Mode Matching

Once the UV output for a single pass was optimized, the input coupler was reinserted and the cavity was aligned. The angle through the crystal is primarily set by the piezo mirror and first curved mirror, along with the 5-axis aligner. These were left untouched, and the remaining degrees of freedom in the system were used to overlap the trips of the beam around the cavity.

Once the beampaths through the cavity sufficiently overlapped, the improvement in the beam coupling was gauged by measuring the reflected power off the input coupler. To measure the amount of light coupled into the cavity, a photodetector observed the reflection of light off the input coupler. As the resonant power builds in the cavity, light transmitted through the input coupler interferes with the reflected incident beam, and the total reflected beam

power decreases (Eq. 2.47). The piezoelectric actuator was driven with a triangle wave to change the length of the cavity which swept it through resonance. Figure 3.4 shows the oscilloscope trace as the cavity is swept through multiple resonances. Improving the cavity coupling was performed by adjusting the positions of the mode matching lenses (L1 and L2 in Figure 3.2) to adjust the position of the waist and size.

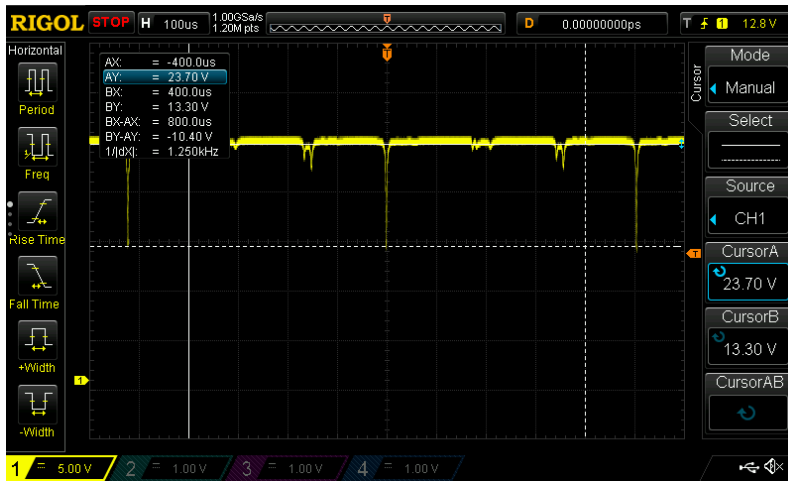


Figure 3.4: Oscilloscope Trace of Scanning Through Resonance. The large, narrow dips in power correspond to the piezo sweeping through resonance of the Gaussian mode. The smaller dips are higher order modes becoming resonant in the cavity. This figure displays close to the maximum amount of input light which was coupled in (45%).

The maximum UV output power measured was $315 \mu\text{W}$. This was measured through the two additional output couplers to isolate the UV light as was done for measuring the UV light for single pass. The circulating power in the cavity was calculated by measuring the blue light transmitted through M3 (Figure 3.2). The transmitted power was $440 \mu\text{W}$, and the reflectivity of this mirror was measured to be .012%. We can determine that 3.6 W of power was

therefore circulating in the cavity, which yields $\gamma = 3.5 \times 10^{-4} \text{ W}^{-1}$. Deviations from γ_{calc} are likely due to the crystal angle not being perfectly aligned, which would increase losses due to phase mis-matching.

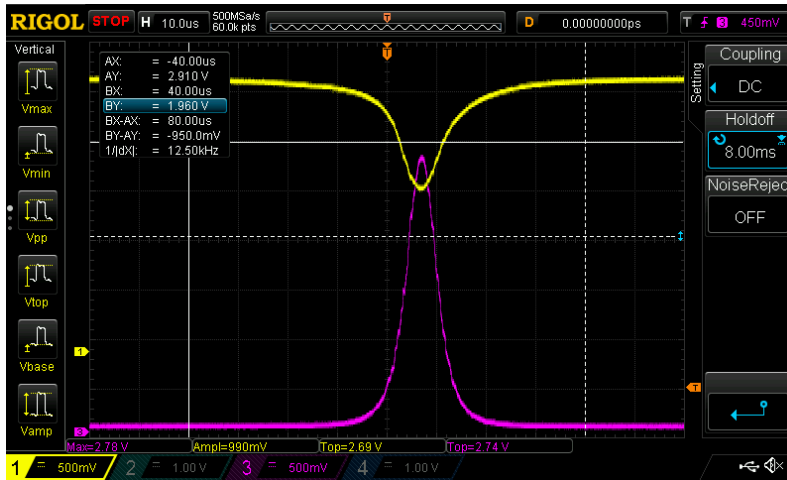


Figure 3.5: Oscilloscope Trace of Blue and UV Buildup. The increase in UV power out (purple trace) is correlated with the buildup in blue light in the cavity (yellow trace), which appears here as the loss of reflected light off the cavity.

Chapter 4

Next Steps

While the laser can produce over $300 \mu W$ of 235 nm light, the potential output is much greater. This section turns an eye towards the future, and discusses the prospects of photoionizing beryllium and necessary steps increase the performance and reliability of the system of the system, including improved mode matching, locking the cavity via the Pound-Drever-Hall technique, and stabilizing the laser frequency.

4.1 Theoretical Rate for Photoionizing Beryllium with the Present Power Output

Attempts to ionize and load ions will be made once the cavity is locked and producing continuous ultraviolet light. With the present power output of the laser, we can determine the expected rate of producing ions. The Einstein A coefficient for the $2s$ to $2p$ transition is $5.52 \times 10^8 \text{ s}^{-1}$ [10], which can be used

to calculate the saturation intensity from [22]

$$I_{sat} = \frac{\pi h c A}{3 \lambda^3}, \quad (4.1)$$

which gives $8.86 \times 10^3 \text{ W/m}^2$ for this transition. With $315 \text{ } \mu\text{W}$, the beam needs to be focused down to a waist of $100 \text{ } \mu\text{m}$ in the trap in order to achieve this saturation intensity. This is a reasonable size to focus a beam down to, so adding more power will not produce significant improvements. However, the second step of the photoionization process occurs much more slowly, as the cross section is $2 \times 10^{-21} \text{ m}^2$ [23]. The cross section of the $2s$ to $2p$ transition is calculated from,

$$\sigma_0 = \frac{1}{4} \frac{g_2}{g_1} \lambda_{21}^2 A_{21}, \quad (4.2)$$

where g_2 and g_1 are the degeneracies of the transition. This gives $2.6 \times 10^{-14} \text{ m}^2$, which is 7 orders of magnitude smaller than the cross section for the $2s$ to $2p$ transition. An increase in the power output will improve the rate of this process. Other systems using around 3 times less power have shown a loading rate of about one ion per minute [12]. While this is adequate, ideally we would be able to ionize beryllium 10 times faster.

4.2 Improved Cavity Performance

As shown in Figure 3.4, the coupling into the cavity was only 45%. This is due to the input beam not being mode matched to the resonant cavity mode. While initial calculations yielded a pair of lenses which should have been able

to accomplish this, less than 30% of the input beam was able to be coupled in. I began a investigation to find possible reasons why the waist size and position were deviating from what we expected to get, and tried to match the behavior of the system with plausible parameter changes

The initial pair of lenses and their position in relationship to the cavity made the waist size very sensitive to the input spot size of the beam. Additionally, for a large enough spot size, the calculation is unable to determine a separation between the two lenses which can bring the beam to a focus. Our uncertainty in the measured spot size could explain our failure to mode match cavity. See Figure 4.1. Based on this assumption, a new pair of lenses were chosen (200 mm and -50 mm), which resulted in most optimized cavity coupling. The specific pair was chosen due to their relative insensitivity to the input spot size. Calculations showed lens pairs with -25 mm could work but there was a lot of spherical aberration with the large radius of curvature when using this short of a focal length. Additional measurements of the beam size and continued work to optimize the placement of the lenses and alignment of the cavity should yield improved results in the coming weeks.

Once the cavity is optimally coupled, it must be impedance matched. If the losses in the cavity are larger than anticipated, the current 99% input coupler will have to swapped out and 100 mW input, we can expect around 30 mW output of ultraviolet light if we are able to impedance match the cavity with a 99% reflectivity input coupler.

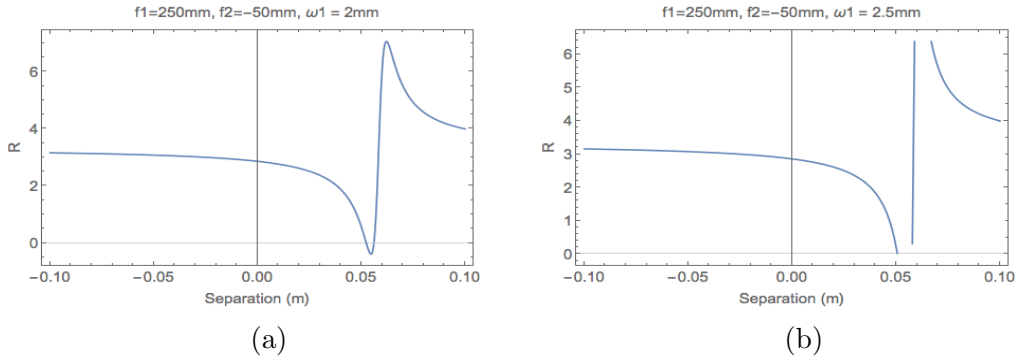


Figure 4.1: Calculations of the required lens separation between a 250 mm lens and -50 mm lens to bring a beam to a focus, varying the distance between the lenses. The left is for an input beam with a 2 mm spot size (approximate input beam size), while the right is for a slightly larger beam at 2.5 mm. For the slightly larger size, there is no configuration where the beam comes to a focus (stable solution for where $R = \infty$.)

4.3 Locking the Cavity

When the cavity second harmonic generation has been optimized, a Pound-Drever-Hall (PDH) locking scheme will be implemented to keep the cavity on resonance by adjusting the length of the piezoelectric actuator [24]. It is also possible to keep stay on resonance by feeding back to the laser and adjusting the wavelength output of the laser to match the length of the cavity, however, because the output light is being used to be resonant with an atomic transition, it is more desirable to keep the laser wavelength constant and dynamically adjust the cavity. The requirements for this Pound-Drever-Hall set the bandwidth specification of the photodetectors which were made.

We can determine when the cavity is on resonance by measuring the power of the reflected beam off the input coupler. As power builds in the resonator, the light reflected off the input coupler (the reflected beam) destructively in-

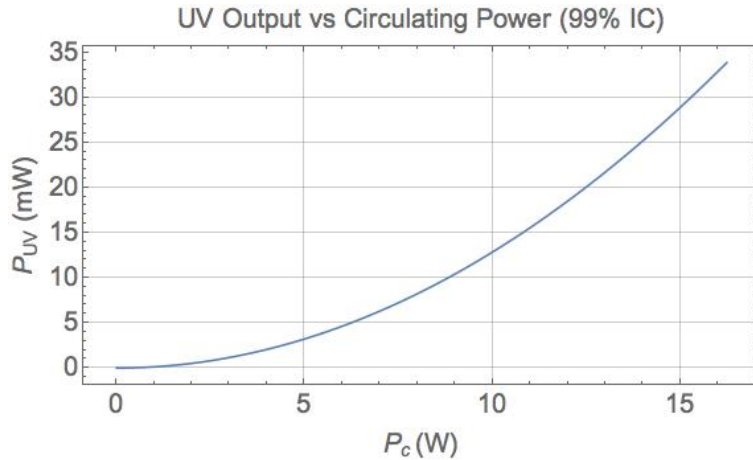


Figure 4.2: Plot of the output 235 nm power versus the circulating cavity power for a cavity on resonance and impedance matched with a 99% input coupler.

interferes with the circulating light leaking through the input coupler (the transmitted beam). If the cavity is perfectly on resonance, these two beams will be equal in intensity, but will be π radians out of phase, so they will destructively interfere completely (Eq. 2.47). As the cavity moves off resonance, the two beams are no longer π radians out of phase, so they fail to completely destructively interfere with each other. It's important to note power reflected as a function of piezo length is an even function. For example, there are two piezo positions (either too long or too short) which correspond to 5% of the reflected beam remaining. Looking at the input power directly is a poor error signal, because the servo would have to guess which direction to adjust the piezo.

The Pound-Drever-Hall technique is an elegant solution to this problem. It allows for the relative phase of the reflected to be determined, therefore

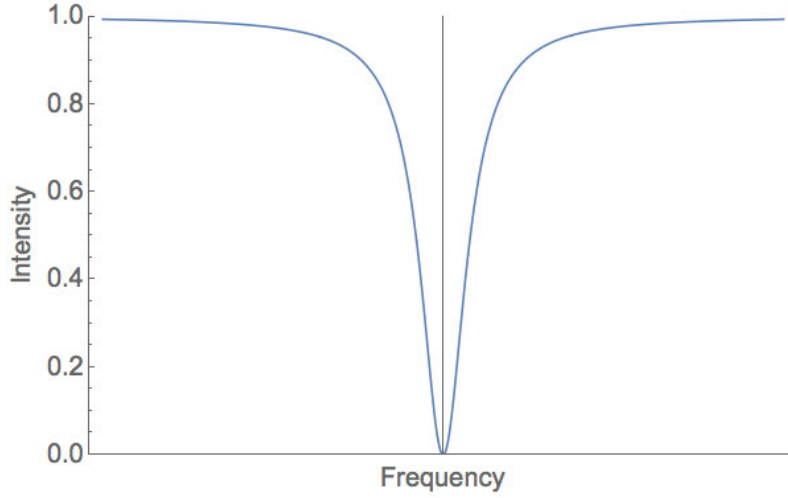


Figure 4.3: Plot of the reflected power versus frequency for a cavity close to resonance.

allowing us to feedback to the piezo to place the cavity back on resonance. Two sidebands are imposed on the main frequency of the laser by modulating its frequency, creating two sidebands, one with a greater frequency and the other a smaller frequency. The interference between the carrier and the sidebands determines which side of resonance the cavity is on, and the sidebands are 180° out of phase. The incident beam, with sidebands, takes the form of

$$E_{inc} = E_0[J_0(\beta)e^{i\omega t} + J_1(\beta)e^{i(\omega+\Omega)t} - J_1(\beta)e^{i(\omega-\Omega)t}] \quad (4.3)$$

where ω is the carrier frequency, Ω is the phase modulation frequency, $J()$ are Bessel functions, and β is the modulation depth, which sets the power of the sidebands. The transmitted beam is just at frequency ω (the cavity does not support the sidebands). The interference between the reflected and incident

beam is therefore

$$E_{ref} = E_0[F(\omega)J_0(\beta)e^{i\omega t} + F(\omega + \Omega)J_1(\beta)e^{i(\omega+\Omega)t} - F(\omega - \Omega)J_1(\beta)e^{i(\omega-\Omega)t}], \quad (4.4)$$

where $F(\omega)$ is the reflection coefficient, the ratio of the reflected to the incident field at the frequency ω . The photodetectors used to measure the reflected light measure power, not the electric field, so to make this relevant we need to convert between the two, and the relationship is $P = |E_0|^2$. The reflected power therefore is

$$\begin{aligned} P_{ref} = & P_c|F(\omega)|^2 + P_s[|F(\omega + \Omega)|^2 + |F(\omega - \Omega)|^2] \\ & + 2\sqrt{P_cP_s}\{\text{Re}[F(\omega)F^*(\omega + \Omega) - F^*(\omega)F(\omega - \Omega)] \cos(\Omega t) \\ & + \text{Im}[F(\omega)F^*(\omega + \Omega) - F^*(\omega)F(\omega - \Omega)] \sin(\Omega t)\} + (2\Omega \text{ terms}) \end{aligned} \quad (4.5)$$

where $P_c = J_0^2(\beta)E_0^2$ and $P_s = J_1^2(\beta)E_0^2$ (power at the carrier and sideband frequencies respectively). The noteworthy terms are the ones varying with frequency Ω . These are from the interference between the carrier and the sidebands. When the modulation frequency is high enough (the regimes between low and high modulation frequencies must be separated because in the high frequency regime there is not enough time for the power to stabilize in the cavity), nearly all of the light at the frequency of the sidebands is reflected (no transmitted light interferes with them). When the cavity is close to resonance, $F(\omega)|^2$ goes to zero, and the cosine term becomes purely imaginary

and disappears. The expression for the reflected power simplifies to

$$P_{ref} = 2P_s - 4\sqrt{P_c P_s} \text{Im}\{F(\omega)\} \sin \Omega t \quad (4.6)$$

where the small contribution from the 2Ω terms have been ignored. An approximation of the power gives a linear error term, which is useful for feedback, and is an odd function, so it can determine the side of resonance. It is

$$\epsilon = -\frac{4}{\pi} \sqrt{P_c P_s} \frac{\delta\omega}{\delta\nu}, \quad (4.7)$$

where $\delta\omega$ is the difference in the cavity resonant frequency and the laser frequency, and $\delta\nu$ is the linewidth of the cavity.

Two photodetectors were designed and built using an in-house PCB design for the purposes of locking the cavity. The first was designed to measure the DC level of the reflected beam. A wedge reflects part of the signal into this photodetector, which uses a biased photodiode to convert the light into a signal. Because the DC level changes rather slowly, bandwidth was not a concern when designing this photodetector, but it is estimated to be around 13MHz, which is more than sufficient to track the power fluctuations in the cavity.

A second detector will monitor the light reflected off the input coupler and be AC-coupled. This detector will have an identical photodiode to the DC coupled detector because of its sensitivity to blue light, but because the intensity of the AC-coupled signal will be much smaller than the DC coupled signal (the variations in the reflected intensity will be small compared to the overall

intensity) and the bandwidth requirements are much higher (the modulation frequency of the laser beam will be around 15 MHz, so the bandwidth of the detector must be well above this). This detector therefore has a two-stage transimpedance amplifier design and uses two amplification stages to increase the bandwidth well above that.

The cavity will be locked with a servo designed for this application [25]. The servo utilizes a field programmable gate array (FPGA), which has both a low latency and is easily reprogrammable via software so the optimal feedback can be given to the piezo. The included software has other features as well, including automatic relocking.

4.4 Laser Frequency Stability

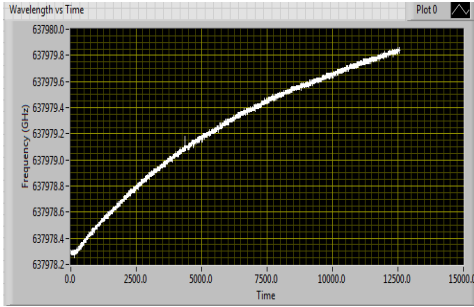
The laser must be kept resonant with the beryllium transition. The linewidth of the transition is assumed to be Doppler broadened, as the atoms have been just vaporized by a hot wire. The full width half maximum of the line is given by

$$\Delta f_{\text{FWHM}} = \sqrt{\frac{8k_B T \ln 2}{mc^2}}, \quad (4.8)$$

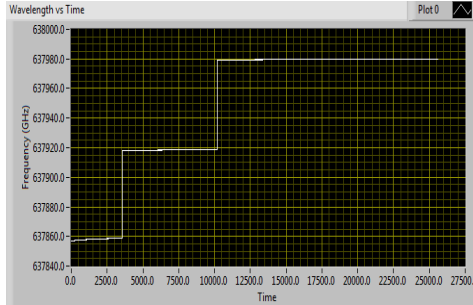
and vaporized beryllium was assumed to be at a few hundred Kelvin, yielding a linewidth of around 10 GHz.

The output of the ECDL was coupled into a fiber optic cable and fed into a wavemeter to measure the frequency. A custom LabView program communicating with the wavemeter recorded and plotted the measurements. The frequency drift over a few hours was observed to exceed the linewidth

of the transition. The mode hops of the laser shown in Figure 4.4 are around 60 GHz, which would take the laser off resonance.



(a) Frequency Measurement over 3.5 Hours



(b) Frequency Measurement over 7 Hours

Figure 4.4: The mode hops displayed by the laser without stabilization will take the laser off the resonant transition of beryllium.

To keep the laser on resonance with the transition, a frequency locking scheme will need to be implemented to provide feedback to the laser to keep it on resonance with the $2s$ to $2p$ transition in beryllium. A stabilized helium neon laser will be used to lock the length of a Fabry-Perot cavity [26]. Part of the 470 nm beam will be directed into the cavity as well and be on resonance in the cavity. The transmission through the cavity of the 470 nm beam will then be monitored to determine if it is resonant with the cavity. If it drifts off resonance, a feedback loop will adjust the current of the laser so the frequency is stabilized.

4.5 Conclusion

The present 235 nm power output of the system is $315 \mu\text{W}$. Ionizing and loading beryllium into the trap is well within reach with the current UV pro-

duction. With improvements in coupling light into the optical resonator and adjustments to the crystal angle, the optimal output should be around 25 mW. These time-intensive operations should occur within a few weeks. At the optimal power, ions could be loaded at a rate much faster than in the noted literature. The measured efficiency of the fundamental to second harmonic conversion has closely matched the theoretical prediction, which is promising for the prospect of approaching 25 mW output.

A significant undertaking in this project was designing and building the monolithic cavity. Despite its complexity, cavity was machined successfully, and completing construction by adding the mirror mounts, optics, crystal aligner, and other components was finished as anticipated. Additionally, this design has the potential to be used for other frequency conversion systems in the future. The input optics, laser head, and cavity were all mounted to a compact optical breadboard. The relative portability of the design should prove fruitful in the future (RIP Merrill). The anticipated vibration tolerance of the monolithic cavity, combined with the frequency stabilization system, should make this system very reliable. This is important, as it will be an important piece in the larger puzzle moving forward. Not only will this laser be responsible ionizing beryllium, but will also assist in determining the state of the diatomic oxygen molecules in the trap in conjunction with Alex Frenett's time-of-flight mass spectrometer. Within a few years, with these and additional systems completed, measuring the time variation of the proton-to-electron mass ratio will proceed.

Appendix A

Monolithic Cavity Design

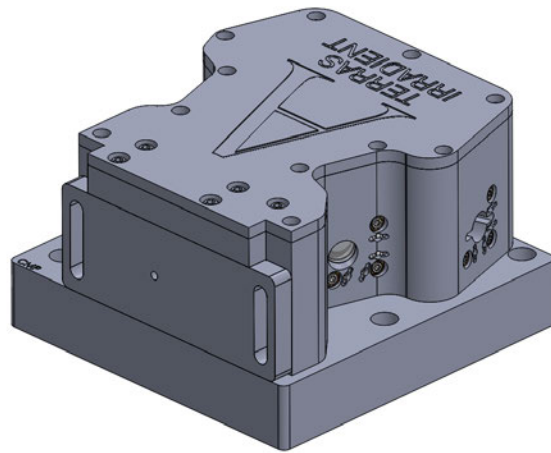


Figure A.1: SolidWorks rendering of the cavity. The thickness of the base was adjusted so that the center of the mirrors in the cavity are at the same height of the beam emitted from the aperture of the ECDL. The lid helps seal the cavity from contaminants, which may adhere to the optics. The base is 6 inches wide by 6 inches tall.

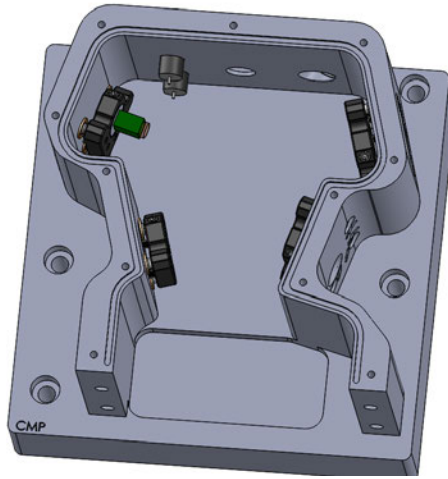


Figure A.2: The crystal aligner has been removed from the SolidWorks model, exposing the pocket in the cavity floor to allow the crystal aligner to move through its entire range of motion.

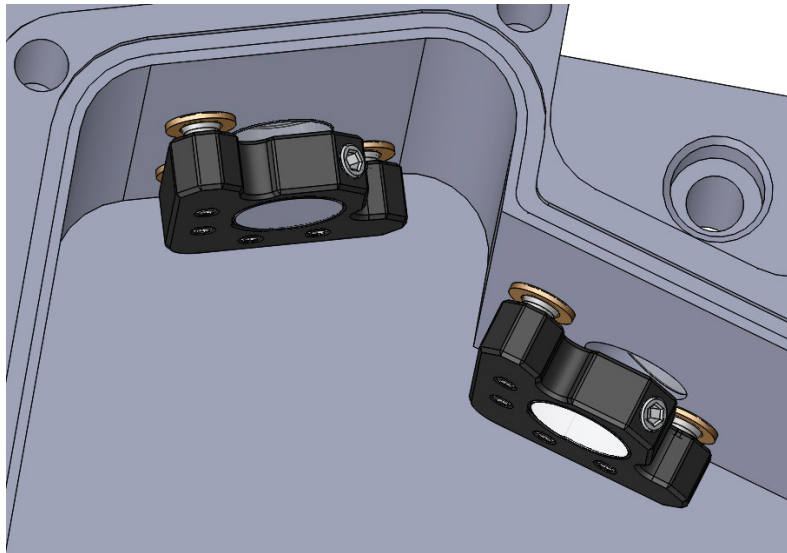


Figure A.3: SolidWorks rendering of the cavity's internal design. The mirror mounts were offset from the cavity wall in the model. The mirrors are offset from the wall in the real implementation so their angle can be changed. Also visible is the O-ring groove which helps provide an airtight seal for the cavity.

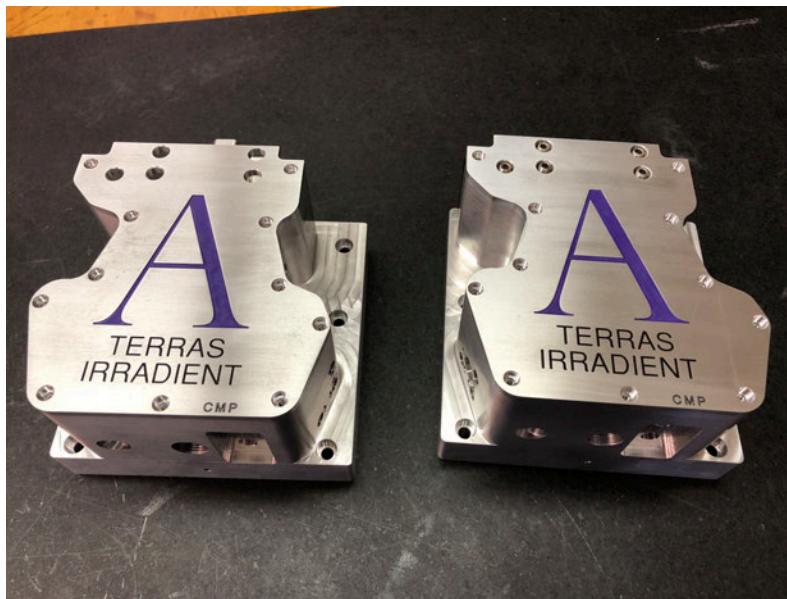


Figure A.4: The pair of cavities machined by Jim Kubasek in the Amherst Machine Shop. The lids have holes for screws to fasten the lid and main body together. There are also holes to access the crystal aligner adjustment knobs without taking off the lid. Minus the lid, the entire cavity was machined from a single block of aluminum.



Figure A.5: BBO sitting in the custom mount, machined by Jim Kubasek. A small pocket was cut for the crystal to rest in, and the two-screw clamp holds it in place. The mount attaches directly to a stock Newport 9081 5-Axis aligner. A small piece of O-ring was placed between crystal and metal clamp to reduce mechanical stress on the crystal, which could induce unwanted birefringence.

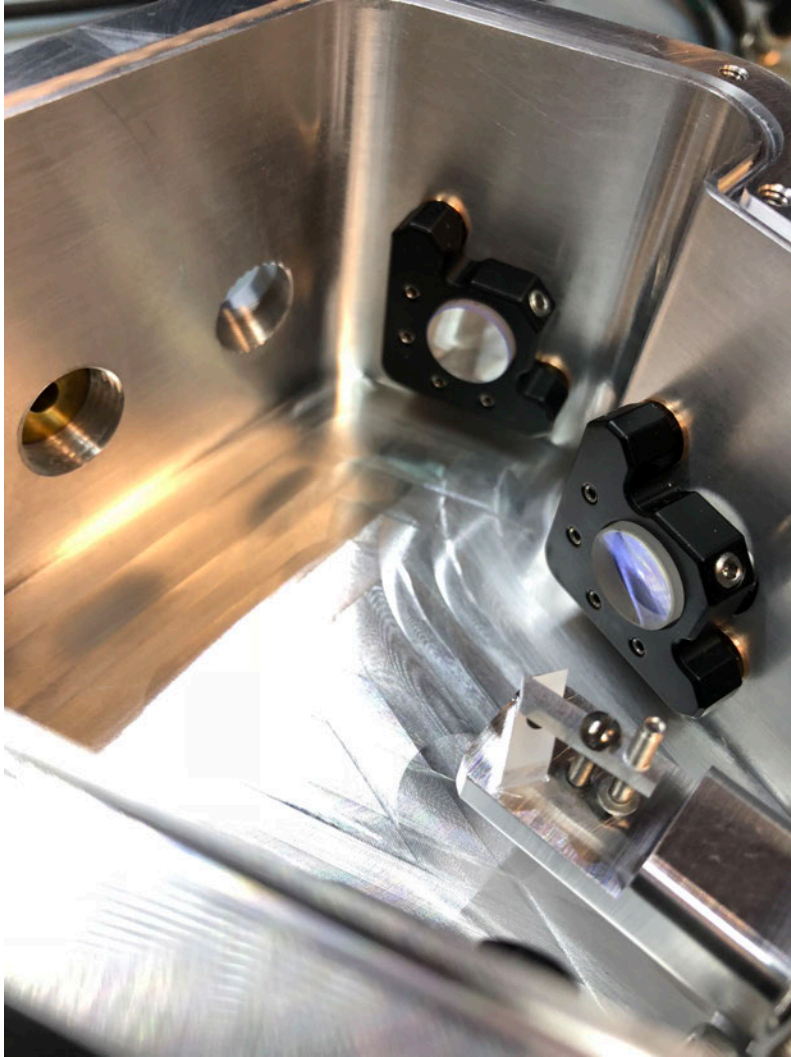


Figure A.6: Internal view of the cavity with the mirror mounts with mirrors installed. Also visible is the hole for the 235 nm light which reflects off the Brewster's cut of the crystal to exit the cavity. The hole is angled with respect to the cavity wall so allow the Brewster reflection to egress. It is also threaded for optics retaining rings to add a window.

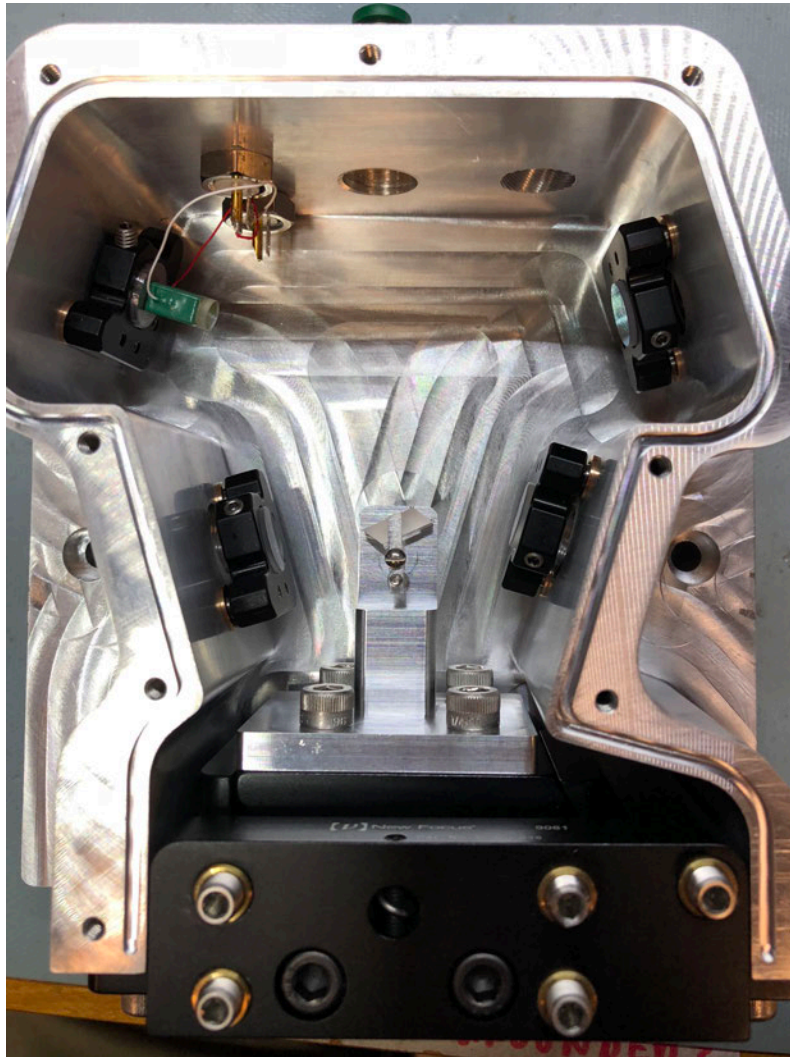


Figure A.7: Top view of the cavity, with the installed optics, crystal and crystal aligner, piezo and BNC connectors, and port for clean air displayed.



Figure A.8: Exterior of the cavity showing the Thorlabs KS-05 mirror mount attached to the cavity wall. The exterior wall serves as the mirror mount backplate, and the stock bushings were replaced. Small holes were made so the Dowel pins can sit recessed into the cavity. The window holes were threaded so that standard lens mounts could hold the windows in place. Also visible is the extra “ears” cut which was added so the incident and reflected beam off the input coupler had enough clearance to make it in and out of the cavity.

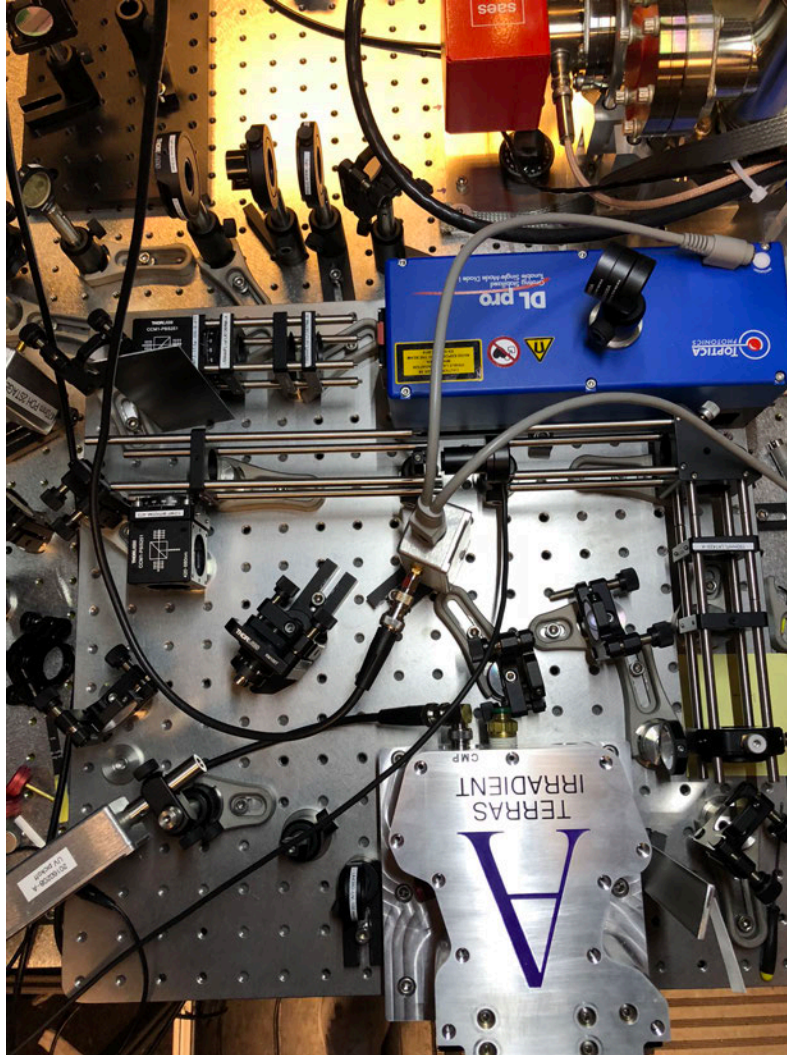


Figure A.9: Cavity along with the other pieces of the laser system, including the ECDL laser head, input optics, and photodetector for measuring the reflection off the input coupler, all mounted to the same optical breadboard. The breadboard will support additional components for locking and fibers optic cables to feed to the frequency stabilization system.

Bibliography

- [1] M. D. Barrett et al. “Sympathetic cooling of $^9\text{Be}^+$ and $^{24}\text{Mg}^+$ for quantum logic”. In: *Phys. Rev. A* 68 (2003), p. 042302. DOI: 10.1103/PhysRevA.68.042302.
- [2] D. J. Wineland et al. “Quantum information processing with trapped ions”. In: *Phil. Trans. R. Soc. Lond. A* 361 (2003), pp. 1349–1361. DOI: 10.1098/rsta.2003.1205.
- [3] C. W. Chou et al. “Optical Clocks and Relativity”. In: *Science* 329 (2010), pp. 1630–1633. DOI: 10.1126/science.1192720.
- [4] Wolfgang Paul. “Electromagnetic traps for charged and neutral particles”. In: *Rev. Mod. Phys.* 62 (1990), pp. 531–540. DOI: 10.1103/RevModPhys.62.531.
- [5] David DeMille, John M. Doyle, and Alexander O. Sushkov. “Probing the frontiers of particle physics with tabletop-scale experiments”. In: *Science* 357 (2017), pp. 990–994. ISSN: 0036-8075. DOI: 10.1126/science.aal3003.

- [6] W. Ubachs et al. “Colloquium: Search for a drifting proton-electron mass ratio from H_2 ”. In: *Rev. Mod. Phys.* 88 (2016), p. 021003. DOI: 10.1103/RevModPhys.88.021003.
- [7] Jean-Philippe Uzan. “The fundamental constants and their variation: observational and theoretical status”. In: *Rev. Mod. Phys.* 75 (2003), pp. 403–455. DOI: 10.1103/RevModPhys.75.403.
- [8] Y. V. Stadnik and V. V. Flambaum. “Can Dark Matter Induce Cosmological Evolution of the Fundamental Constants of Nature?” In: *Phys. Rev. Lett.* 115 (2015), p. 201301. DOI: 10.1103/PhysRevLett.115.201301.
- [9] D. Hanneke, R. A. Carollo, and D. A. Lane. “High sensitivity to variation in the proton-to-electron mass ratio in O_2^+ ”. In: *Phys. Rev. A* 94 (2016), 050101(R). DOI: 10.1103/PhysRevA.94.050101.
- [10] A. Kramida et al. NIST Atomic Spectra Database (ver. 5.5.2), [Online]. Available: <https://physics.nist.gov/asd> [2018, February 6]. National Institute of Standards and Technology, Gaithersburg, MD. 2018.
- [11] Ryan A. Carollo et al. “Third-harmonic-generation of a diode laser for quantum control of beryllium ions”. In: *Opt. Expr.* 25 (2017), pp. 7220–7229. DOI: 10.1364/OE.25.007220.
- [12] Hsiang-Yu Lo et al. “All-solid-state continuous-wave laser systems for ionization, cooling and quantum state manipulation of beryllium Ions”. In: *Appl. Phys. B* 114 (2014), pp. 17–25. DOI: 10.1007/s00340-013-5605-0.

- [13] S. Hannig et al. “A highly stable monolithic enhancement cavity for SHG generation in the UV”. In: *arxiv* (2017). DOI: 10.1063/1.5005515.
- [14] Warren Nagourney. *Quantum Electronics for Atomic Physics*. Oxford University, 2010.
- [15] Anthony E. Siegman. *Lasers*. University Science Books, 1986.
- [16] Weng W. Chow, Stephan W. Koch, and Murray Sargent III. *Semiconductor Laser Physics*. Springer-Verlag, 1994.
- [17] Bela Lengyel. *Lasers*. Second. Wiley-Interscience, 1971.
- [18] TOPTICA Photonics. *DL Pro Datasheet*.
- [19] Robert W. Boyd. *Nonlinear Optics*. Academic Press, 1992.
- [20] G. D. Boyd and D. A. Kleinman. “Parametric Interaction of Focused Gaussian Light Beams”. In: *J. Appl. Phys.* 39 (1968), pp. 3597–3639.
- [21] Laseroptik. *Laseroptik HT235 HR470 Coating Datasheet*.
- [22] Robert C. Hilborn. “Einstein coefficients, cross sections, f values, dipole moments, and all that”. In: *American Journal of Physics* (2002).
- [23] Dae-Soung Kim et al. “Photoionization of the excited $1s^2 2s 2p^{1,3} P^o$ states of atomic beryllium”. In: *Phys. Rev. A* 64 (4 2001), p. 042713. DOI: 10.1103/PhysRevA.64.042713.
- [24] Edward K. Kleiner. “Quantum Control of Be^+ Ions”. Undergraduate thesis. Amherst College, 2016.

- [25] D. R. Leibbrandt and J. Heidecker. “An open source digital servo for atomic, molecular, and optical physics experiments”. In: *Rev. Sci. Instrum.* 86 (2015), p. 123115. DOI: 10.1063/1.4938282.
- [26] Chu Cheyenne Teng. “Frequency Control and Stabilization of a Laser System”. Undergraduate thesis. Amherst College, 2013.